Scattering under Grazing Incidence from Surfaces and Interfaces

U. Rücker

This document has been published in

Manuel Angst, Thomas Brückel, Dieter Richter, Reiner Zorn (Eds.):
Scattering Methods for Condensed Matter Research: Towards Novel Applications at Future Sources
Lecture Notes of the 43rd IFF Spring School 2012
Schriften des Forschungszentrums Jülich / Reihe Schlüsseltechnologien / Key Technologies, Vol. 33
JCNS, PGI, ICS, IAS
Forschungszentrum Jülich GmbH, JCNS, PGI, ICS, IAS, 2012
ISBN: 978-3-89336-759-7

D 2 Scattering under Grazing Incidence from Surfaces and Interfaces

U. Rücker
Jülich Centre for Neutron Science
Forschungszentrum Jülich GmbH

Contents

Lecture Notes of the 43rd IFF Spring School "Scattering Methods for Condensed Matter Research: Towards Novel Applications at Future Sources" (Forschungszentrum Jülich, 2012).

1 Motivation

During the last decades, the possibility to create structures confined along one or more dimensions to a size in the nanometer range has induced a class of materials with extraordinary properties, as well from the scientific as from the technological points of view. Beginning from Si based integrated circuits over layered magnetic structures showing the Giant Magnetoresistance (GMR) effect [1] to displays out of conducting polymers produced by ink-jet technology [2], layered structures use the interface effects on the conducting electrons and (in the case of magnetic structures) on the electron spin.

For a complete understanding of the properties of a layered structure the approximation of laterally homogeneous layers with sharp boundaries generally does not hold. For example in the case of the magnetic exchange coupling between a ferromagnetic and an antiferromagnetic layer, which leads to a shift of the hysteresis loop of the ferromagnetic layer ("exchange bias"), the measured effect is two orders of magnitude weaker than the calculated effect based on the assumption of a magnetic structure in the antiferromagnet which is not affected by the interface. The up-to-date models need to take into account monoatomic steps at the interface between ferromagnet and antiferromagnet and formation of magnetic domains inside the antiferromagnet [3,4,5].

Like this, there are many examples of effects in thin film structures, e.g. chemical segregation, magnetic interlayer coupling, tunnelling magnetoresistance, proximity effects, spin injection, etc., where it is important to be able to investigate the chemical and magnetic structure in the inner layers of the sample. Most of the methods used to investigate thin film structures either integrate over the sample (e.g. SQUID magnetometry), are purely surface sensitive (e.g. Scanning Tunneling Microscopy STM, Atomic Force Microscopy AFM, Magnetic Force Microsopy MFM, Low Energy Electron Diffraction LEED) or integrate over a certain depth (e.g. Auger Electron Spectroscopy AES, Kerr microscopy). Some methods are element specific (e.g. Photoemission Electron Microscopy PEEM) without pronounced depth sensitivity, so they allow to distinguish between different layers consisting of different elements, but not to distinguish between several layers with identical composition, e.g. between the two Fe layers in a Fe / Cr / Fe trilayer.

For a specific access to the buried interfaces or layers, we need to use a probe that can penetrate the sample and that is coherent over the size of the objects of interest to be able to detect the interference between signals from different depth. Useful probes are x-ray photons as well as neutrons, because they can penetrate solid samples and have wavelengths in the order of a few Å, suitable to resolve structures of atomic size.

Generally, in thin film research, the atomic structure of the layers is not subject to the investigation, but the layer structure and inhomogeneties of the layers, e.g. growth islands, density fluctuations, magnetic domains or interdiffusion regions.

To resolve layer structure, vertical interface profiles and interdiffusion regions, one needs a resolution in the z-direction of the order of a fraction of the layer thickness. As layer thicknesses vary from atomic monolayers to several 100 nm, a z-resolution in the order of Å to µm is needed.

In the lateral direction, i.e. parallel to the film plane, different structures are of interest. It starts with lithographically produced structures in the µm range, grains in polycrystalline layers (1000 to 50 nm), growth islands (100 nm to 10 nm) and goes down to self-organized lateral structures (down to 1 nm). Sometimes, e.g. in self-organized nanoparticle arrays deposited on a substrate, several length scales are of importance. The internal structure of the array (i.e. the periodicity of the nanoparticle arrangement) is in the range of several nanometers, while the size distribution of the domains of coherent structure or the clusters of nanoparticles can extend up to several micrometers. All these length ranges are accessible with scattering under grazing incidence.

2 Specular reflectivity and scattering under grazing incidence

The investigation of structure and interfaces of thin films with x-rays or neutrons is mostly performed using elastic scattering under grazing incidence. In this case, a monochromatic, well collimated beam impinges under a well defined, small angle $\alpha_i = \theta$ (in most cases $\theta << 5°$) onto the surface of the sample. It is then partly reflected specularly from the surface, i.e. the outgoing angle $\alpha_f = \theta$ as well, and partly refracted into the material (see Fig. 1). As I will derive in section 4, the reflection of x-rays or neutrons from a laterally homogeneous medium can be treated according to classical optics. Only the proper index of refraction n for the radiation has to be used.

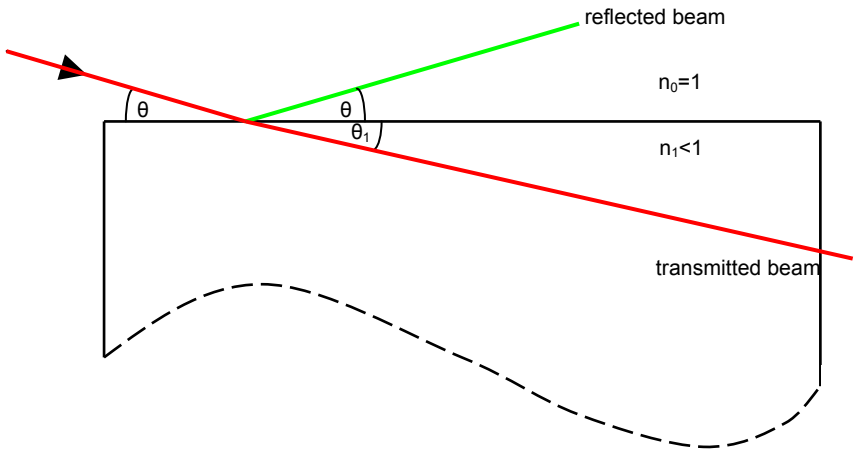

Fig. 1: *Reflection and Refraction from a free surface*

For most materials, the index of refraction for neutrons and x-rays is slightly smaller than 1, leading to total external reflection for small angles of incidence $\theta < \theta_c$, where θ_c depends on the material and the radiation.

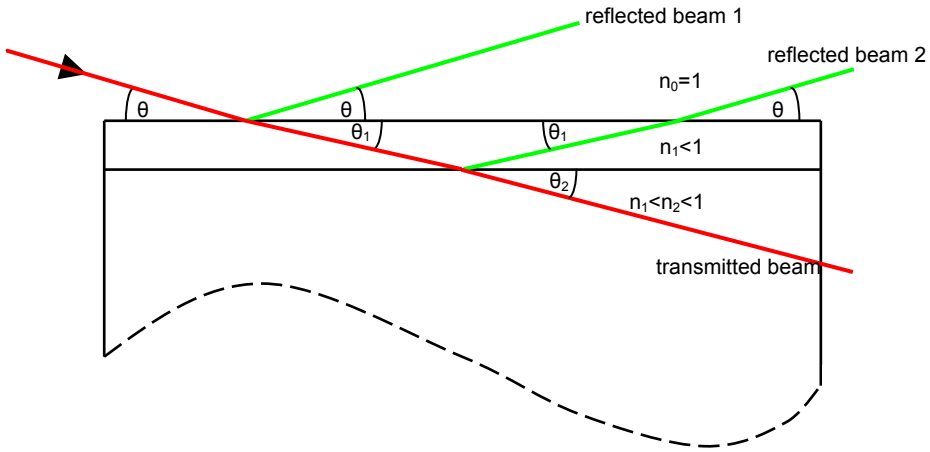

Fig. 2: *Reflection and Refraction from a single layer on a substrate*

In the case of a single layer on the substrate, reflection and refraction take place at both the surface and the interface (Fig. 2). Then, the reflected beams from the different interfaces interfere with each other. Maximum intensity is received, when the path length difference between the two reflected beams is an integer multiple of the wavelength. Due to the continuity relation of the wave function at the interfaces, the intensity of the transmitted beam is modulated opposite to the reflected beam. Fig. 10 shows the reflectivity curve of a real single layer on a substrate. It is discussed in detail in chapter 5.1.

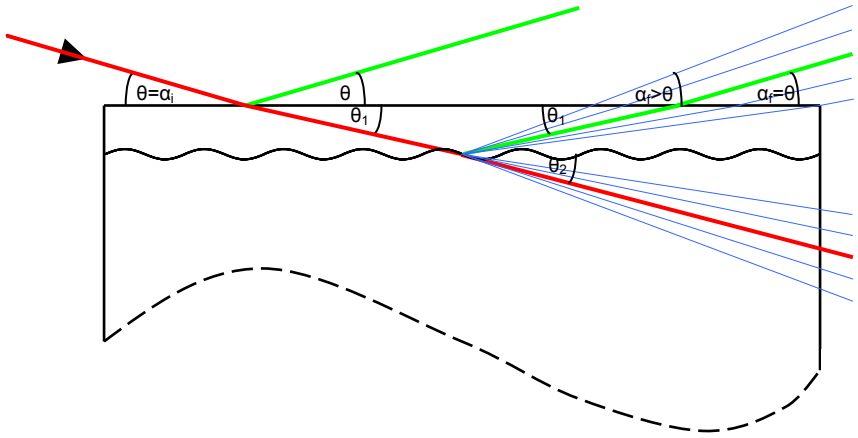

Fig. 3: *Specular and off-specular scattering from a laterally modulated interface*

If surface and interface are laterally ideally homogeneous and flat, the complete beam is either reflected specularly or transmitted after refraction. If the interface is not flat, but e.g. periodical (as sketched in Fig. 3), additional beams are coming up. Their origin is diffraction from the modulated interface, as it is known from an optical grating. This so-called off-specular or diffuse scattering can be observed at $\alpha_f \neq \alpha_i$.

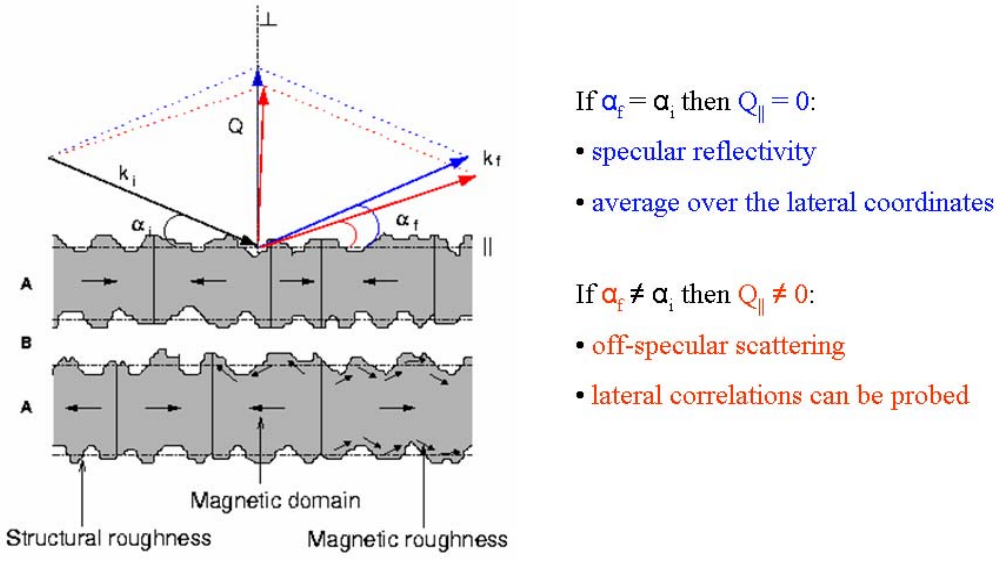

Fig. 4: *General geometry of reflectivity and off-specular scattering*

The general principle of a scattering experiment under grazing incidence is depicted in Fig. 4 and the exact geometry is given in Fig. 5. For the mathematical description of the scattering process, it is again convenient to introduce the wave vectors $\mathbf{k_i}$ and $\mathbf{k_f}$ for the incoming and the detected wave, respectively. Neutrons or x-rays impinge on the sample surface under the grazing angle of incidence α_i with wave vector $\mathbf{k_i}$ and are detected with outgoing wave vector $\mathbf{k_f}$ whose direction is defined by the angle α_f in the plane of incidence and by the angle φ perpendicular to it. Let $\mathbf{Q} = \mathbf{k_f} - \mathbf{k_i}$ be the scattering wave vector and $\mathbf{Q}_{//} = (Q_x,Q_y,0)$ its component in the sample plane. I will restrict the discussion to elastic scattering, i.e. $k_i = k_f = 2\pi / \lambda$ where λ is the wavelength of the radiation.

If the sample can be considered as laterally homogeneous, i.e. invariant by translation along its surface, intensity can only be observed in the specular direction defined by $\mathbf{Q}_{//} = 0$, i.e. at $\alpha_f = \alpha_i$ and $\varphi = 0$. If the sample shows lateral fluctuations like chemical roughness, magnetic roughness or magnetic domains, then some intensity can be observed in the directions given by $\mathbf{Q}_{//} \neq 0$, i.e. by $\alpha_f \neq \alpha_i$ and $\varphi \neq 0$. Very often specular reflectivity and scattering under grazing incidence are observed simultaneously. Specular reflectivity then gives information

on the order parameters averaged over the lateral coordinates and diffuse scattering gives access to the fluctuations around this mean value.

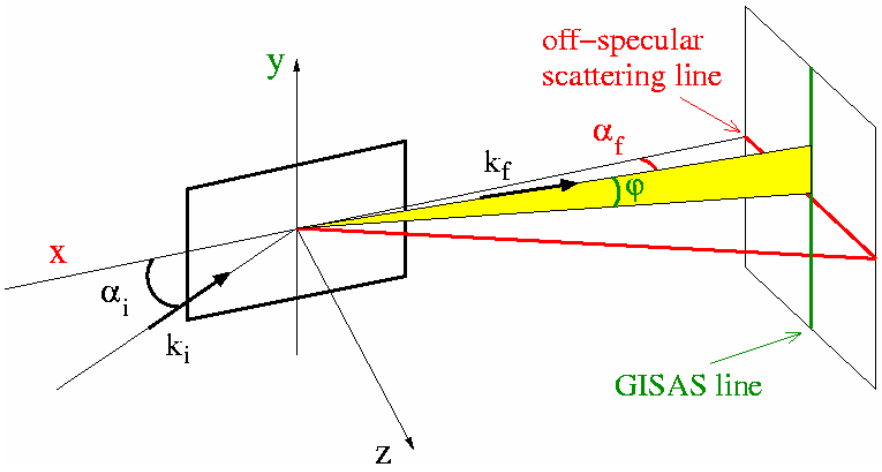

Fig. 5: *The different geometries of scattering under grazing incidence. Off-specular scattering probes lateral correlations along the x-direction, while grazing incidence small angle scattering (GISAS) probes correlations along the x- and y-directions.*

In practice, two types of scattering under grazing incidence geometries can be used (Fig. 5). The first one is obtained by scanning α_i and α_f while integrating the measured intensities along φ. This is called off-specular scattering. For the second one, the experimental conditions are such that φ can be resolved. Recording the intensities along φ as a function of α_i and α_f is called grazing incidence small angle scattering (GISAS).

Taking into account the small values of the angles α_i, α_f and φ, the scattering wave vector projects itself on the three axis of the coordinate system of Fig. 5 in the following manner:

$$\mathbf{Q} = \begin{cases} Q_x \approx k \cdot (\alpha_i^2 - \alpha_f^2 - \varphi^2) \\ Q_y \approx k \cdot \varphi \\ Q_z \approx k \cdot (\alpha_i + \alpha_f) \end{cases} \qquad (1)$$

Note that while Q_x is a linear combination of squares of small angles, Q_y is linear in φ. Q_x is then always much smaller than Q_y. Typically, at a neutron source one has 0.5 µm < $d_x = 2\pi/Q_x$ < 20 µm and 1 nm < $d_y = 2\pi/Q_y$ < 300 nm. The lower limits are defined by the maximum available intensity and the upper limits are fixed by the reachable resolution in Q_x and Q_y. It appears then that GISANS (grazing incidence small angle neutron scattering) probes much smaller length scales than off-specular scattering. For x-rays the lower limits for d_x and d_y can

be brought even smaller thanks to the availability of high intensity synchrotron sources. As GISAS gives access to the nanometer length scale in the sample plane, one observes at the moment a rush on this method, with both neutrons (GISANS) and x-rays (GISAXS).

Off-specular and GISAS intensities are represented differently, because they have a different dimension. The 3-dimensional off-specular data are typically represented as a function of α_i and α_f with a colour encoding of the intensity (Fig. 6a). Along the main diagonal where $\alpha_i = \alpha_f$ is the specular line ($Q_x = 0$). Out of this diagonal, off-specular scattering is measured and the lateral correlations are probed along the x-direction ($Q_x \neq 0$). Along lines perpendicular to the specular line where $\alpha_i + \alpha_f$ = constant, the correlations are probed along Q_x at Q_z constant (cf. eq. (1)).

GISAS measurements are 4-dimensional and therefore cannot be displayed in a single figure containing all data. As the experiments are usually performed on a small angle scattering instrument [6] where the data is collected on the 2D position sensitive detector, it is a common way to present the measurements at fixed α_i. For a well defined angle of incidence α_i and a well defined sample-to-detector distance, the intensities recorded on the 2D detector give the GISAS signal as a function of $\alpha_i + \alpha_f$ and φ (Fig. 6b). As $Q_y \approx k \cdot \varphi$, the φ axis directly gives access to the correlations along the y-axis. The specular reflectivity peak can be found at the coordinate ($\alpha_i + \alpha_f = 2\,\alpha_i$, $\varphi = 0$).

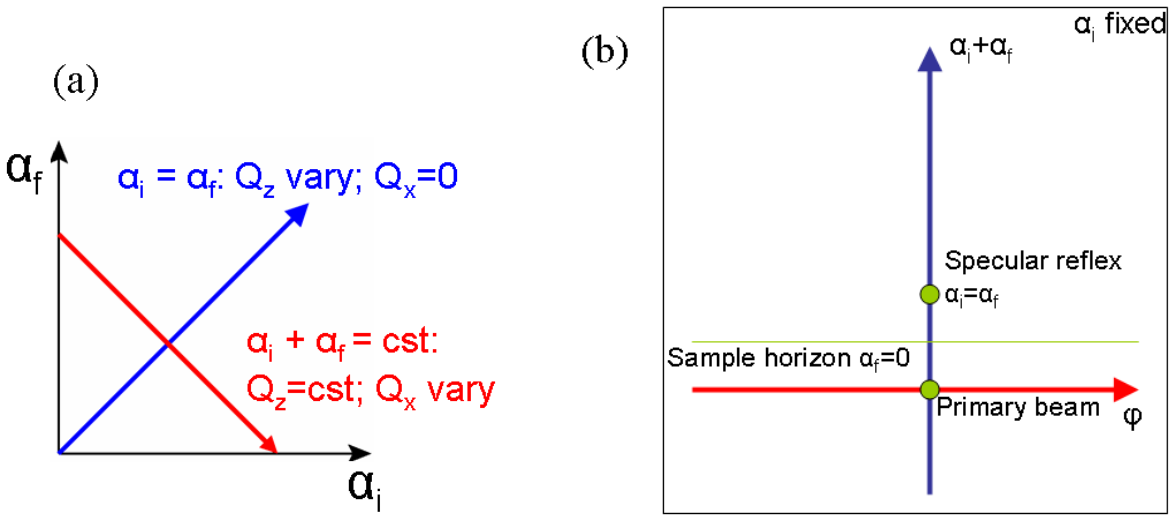

Fig. 6: *Data representation of off-specular scattering (a) and GISAS (b)*

3 Spatial coherence of the beam

An important quantity to consider in the interpretation of specular reflectivity and scattering under grazing incidence is the coherence volume of the beam [7], because its projection S_{coh} on the sample surface, while sometimes large enough to induce multiple scattering effects, stays smaller than the illuminated part of the sample surface. This is always true for a neutron beam. At shallow angles it might not be true for a x-ray beam at a synchrotron source, because of the high spatial coherence of the x-ray beam due to the large distance of the source with respect to the sample, its small lateral size and the good wavelength resolution. In that case, the surface of coherence is the entire illuminated part of the sample surface.

$$S_{coh} = L^{x}_{coh} \cdot L^{y}_{coh} \tag{2}$$

is connected to the resolutions of the in-plane components of the scattering wave vector

$$L^{x}_{coh} \propto 1/\delta Q_x \quad \text{and} \quad L^{y}_{coh} \propto 1/\delta Q_y . \tag{3}$$

which themselves depend on the quality of monochromatization (wavelength spread) of the beam and the angular divergence. These values always depend on the instrument used and the settings of the slits etc. that should be optimized for the specific experiment.

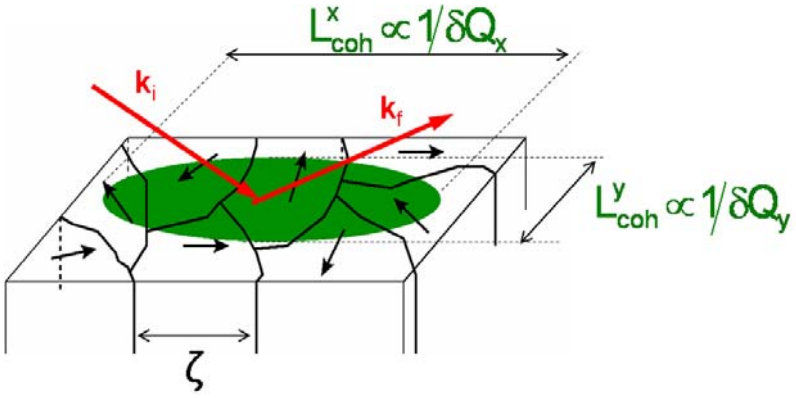

Fig. 7: *Projection of the coherence volume of the beam on the sample surface. The surface thus obtained has the lateral dimensions* L^{x}_{coh} *and* L^{y}_{coh} *along the x- and y-directions of Fig. 5. In order to interpret correctly the measured data, those lengths have to be compared with the correlation length* ζ *of the lateral fluctuations.*

If, within S_{coh}, the sample consists of homogeneous layers with flat interfaces, there cannot be any transfer between the in-plane components of $\mathbf{k}_i$ and $\mathbf{k}_f$ and intensity is observed only along the specular direction defined by $\mathbf{Q}_{//} = \mathbf{0}$ with a precision given by $\delta\mathbf{Q}_{//}$. The measured reflectivity is therefore an average over all the reflectivities generated by all the surfaces of coherence that compose the surface of the sample and for which the homogeneous and flat approximation holds. Therefore, the absence of scattering under grazing incidence is not always due to the fact that the sample is homogeneous and flat over its whole surface.

If, on the contrary, the system is not invariant by a lateral translation along the x or y direction by a vector whose modulus is smaller than L^x_{coh} or L^y_{coh}, respectively, a transfer of momentum parallel to the surface can take place ($\mathbf{Q}_{//} \neq 0$) and scattering under grazing incidence can be observed. The scattering cross section is then an average over the scattering cross sections generated by the different surfaces of coherence that compose the sample.

Usually, scattering under grazing incidence and specular reflectivity coexist. Reflectivity comes from the depth variation of the order parameter averaged over the lateral coordinates and scattering under grazing incidence finds its origin in the fluctuations around this mean value.

4 Specular reflectivity: Optical approach

For the case of a perfectly smooth surface, an exact description of the reflected and transmitted intensity can be deduced from quantum theory. This approach is also valid, if the correlation lengths of the fluctuations exceed largely the coherence length in the respective direction.

As an example, I will show the case for neutrons, although the identical calculus is valid for x-rays. Only some nature constants are different, resulting in a different term describing the index of refraction.

The starting point is the Schrödinger equation for the wave function of the neutron

$$\left[-\frac{\hbar^2}{2m}\Delta + V(\mathbf{r})\right]\Psi(\mathbf{r}) = E\Psi(\mathbf{r}) \tag{4}$$

The energy of the neutron is given by $E = \hbar^2 k^2/(2m)$ with the modulus $k = 2\pi/\lambda$ of the wave vector $\mathbf{k}$. As we assume elastic scattering, the energy of the incident and of the outgoing wave is identical.

The resolution of a reflectometry experiment does not resolve the atomic structure of the sample in any of the three directions. Therefore, it is a valid approximation to describe the

potential V_1 of the homogeneous material as the sum of the scattering length densities of all constituents (see lecture A4):

$$V_1 = \frac{2\pi\hbar^2}{m}\sum_j b_j\rho_j \tag{5}$$

where b_j are the coherent scattering lengths and ρ_j the atomic number densities of the different elements (evtl. isotopes) in the material. With that, we receive

$$\left[\Delta + \left(k^2 - 4\pi\sum_j b_j\rho_j\right)\right]\Psi(\mathbf{r}) = \left[\Delta + k^2\left(1 - \frac{\lambda^2}{\pi}\sum_j b_j\rho_j\right)\right]\Psi(\mathbf{r}) = \left[\Delta + k_1^2\right]\Psi(\mathbf{r}) = 0 \tag{6}$$

with the wave vector $\mathbf{k}_1$ inside the medium. From this equation, it is justified to introduce the index of refraction of the material

$$n = \frac{k_1}{k} \qquad n = 1 - \frac{\lambda^2}{2\pi}\sum_j b_j\rho_j =: 1 - \delta \qquad \delta = \frac{\lambda^2}{2\pi}\sum_j b_j\rho_j \tag{7}$$

It is a number very close to 1 for thermal and cold neutrons. The correction δ is called dispersion and is in the order of 10^{-5} to 10^{-6}. For most materials δ is positive (because the coherent scattering length b is positive for most isotopes), so that n is smaller than 1. This means that the transmitted beam is refracted towards the sample surface, which is opposite to the daily experience with light refracted at a glass or liquid surface.

For most materials, such as silicon, aluminium or iron, the absorption of neutrons is negligible. In case, it is not negligible, it can be introduced most straightforward by including an imaginary part to the index of refraction:

$$n = 1 - \delta + i\beta \tag{8}$$

In the case of x-rays the description in the framework of optical refraction inside the material is valid as well. In this case the index of refraction can be calculated as

$$n = 1 - \frac{\lambda^2 r_o}{2\pi}\sum_j \rho_j(Z_j + f_j' + if_j'') =: 1 - \delta + i\beta \qquad \delta = \frac{\lambda^2 r_0}{2\pi}\sum_j \rho_j(Z_j + f_j') \tag{9}$$

r_0 is the classical electron radius $r_0 = e/m_e c^2 = 2.82$ fm, Z is the number of electrons of the atom and f' and f'' are corrections for dispersion and absorption close to resonance energies. Typically, they can be neglected, only at the absorption edges they become important. An example for contrast variation close to the resonances is given in section 5.3.
Also for x-rays, the dispersion δ is always positive, so that the index of refraction n is smaller than 1.

In analogy to classical optics, we can derive e.g. Fresnel's formulas: For the solution of the wave equation at the sharp interface, we assume the surface of the sample to be at z = 0. The potential is then

$$V(z) = \begin{cases} 0 & \text{for } z > 0 \\ V_1 & \text{for } z \le 0 \end{cases} \tag{10}$$

As the potential is independent on x and y, the wave vector $\mathbf{k}_l$ in the wave equation (6) is also independent on x and y. Therefore, the wave equation can be separated by the Ansatz

$$\Psi(\mathbf{r}) = \Psi_x(x)\Psi_y(y)\Psi_z(z) \tag{11}$$

For the z direction we receive the one-dimensional differential equation

$$\Psi_z''(z) + k_z^2(z)\Psi_z(z) = 0 \tag{12}$$

To solve the differential equation we use the Ansatz

$$\Psi_{zl}(z) = t_l e^{ik_{zl}z} + r_l e^{-ik_{zl}z} \tag{13}$$

The index l distinguishes between vacuum (l=0) and matter (l=1). The factors t_l describe the wave field away from the surface, i.e. the transmitted wave, the factors r_l describe the wave field towards the surface, i.e. the reflected wave. The unique solution is determined by the boundary conditions. In a half-infinite medium, there is no reflected wave, because there is nothing to reflect from, i.e. r_l vanishes. In addition, the wave function and its first derivative must be continuous at the interface. So we receive the boundary conditions

$$\begin{aligned} &\Psi_{z0}(z=0) = \Psi_{z1}(z=0) \\ &\Psi_{z0}'(z=0) = \Psi_{z1}'(z=0) \\ &r_1 = 0 \end{aligned} \tag{14}$$

When we insert (14) into (12) and (13), we receive the continuity equations for the wave function

$$\begin{aligned} &t_0 + r_0 = t_1 \\ &k_{z0}(t_0 - r_0) = k_{z1}t_1 \end{aligned} \tag{15}$$

t_0 is the amplitude of the incoming wave, t_1 of the transmitted wave and r_0 of the reflected wave.

We can rewrite this set of equations in a matrix equation

$$\begin{pmatrix} t_0 \\ r_0 \end{pmatrix} = \mathbf{M_0} \begin{pmatrix} t_1 \\ r_1 \end{pmatrix} = \mathbf{M_0} \begin{pmatrix} t_1 \\ 0 \end{pmatrix} \tag{16}$$

The reflectivity R is defined as the ratio of the intensities of reflected and incoming waves, the transmissivity T is defined as the ratio of the intensities of transmitted and incoming waves.

$$R = \left| \frac{r_0}{t_0} \right|^2 \qquad T = \left| \frac{t_1}{t_0} \right|^2 \tag{17}$$

In conclusion, we arrive at Fresnel's formulas for the reflection at a flat interface

$$\text{Reflectivity} \qquad R = \left| \frac{k_{z0} - k_{z1}}{k_{z0} + k_{z1}} \right|^2 = \left| \frac{\theta - n_1 \theta_1}{\theta + n_1 \theta_1} \right|^2 \tag{18}$$

$$\text{Transmissivity} \qquad T = \left| \frac{2k_{z0}}{k_{z0} + k_{z1}} \right|^2 = \left| \frac{2\theta}{\theta + n_1 \theta_1} \right|^2 \tag{19}$$

Taking into account the continuity relation for the wave vector component tangential to the surface

$$k_{x0} = k_{x1} \qquad k_{y0} = k_{y1} \tag{20}$$

together with $k_1 = k_0 n$ (eq. 7), Snell's law for refraction follows from trigonometry:

$$\frac{\cos\theta_0}{\cos\theta_1} = \frac{k_1}{k_0} = n_1 \tag{21}$$

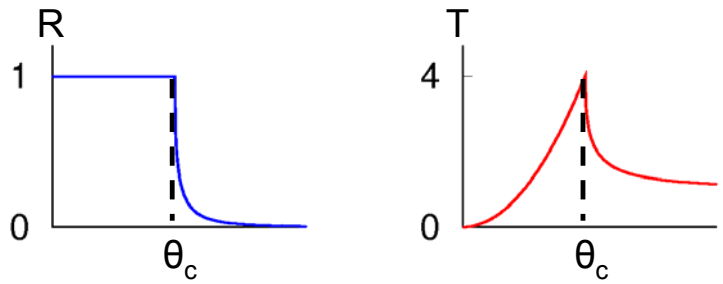

Fig. 8: *Reflectivity and transmittivity as a function of the angle of incidence*

The fact that in most cases the index of refraction is n < 1 means that the transmitted beam is refracted towards the sample surface ($\theta_1 < \theta$ in Fig. 1). For angles of incidence θ below the so-called critical angle θ_c with

$$n = \cos\theta_c \qquad \theta_c \approx \sqrt{2\delta} \tag{22}$$

total reflection is observed, i.e. all intensity is reflected and no wave propagating in z-direction exists in the sample. Only an evanescent wave with propagation parallel to the surface is induced. In this case, t_1 as well as k_{z1} are imaginary numbers. Still, as shown in Fig. 8, the modulus of t_1 is increasing when approaching θ_c. The strong evanescent wave field inside the surface is the origin of the strong offspecular Yoneda scattering close to $\alpha_i = \theta_c$ and $\alpha_f = \theta_c$. For incident angles above θ_c, the beam can partially penetrate the sample and is only partly reflected.

In the case of p layers on a substrate, the same calculus can be used. At every interface, the continuity relation can be formulated analogous to (16):

$$\begin{pmatrix} t_0 \\ r_0 \end{pmatrix} = \mathbf{M_0}\begin{pmatrix} t_1 \\ r_1 \end{pmatrix} \qquad \begin{pmatrix} t_1 \\ r_1 \end{pmatrix} = \mathbf{M}_1\begin{pmatrix} t_2 \\ r_2 \end{pmatrix} \qquad \ldots\ldots \qquad \begin{pmatrix} t_p \\ t_p \end{pmatrix} = \mathbf{M}_p\begin{pmatrix} t_{p+1} \\ 0 \end{pmatrix} \tag{23}$$

The amplitudes of reflected and transmitted wave then can be calculated by a matrix multiplication of the individual reflection matrices:

$$\begin{pmatrix} t_0 \\ r_0 \end{pmatrix} = \mathbf{M_0} \cdot \mathbf{M_1} \cdot \ldots \cdot \mathbf{M_p}\begin{pmatrix} t_{p+1} \\ 0 \end{pmatrix} \tag{24}$$

From equation (18), it becomes obvious, that reflection is only achieved when a difference between the indices of refraction of the adjacent layers exists. If one wants to investigate two layers with neutron or x-ray reflectivity, the contrast of the indices of refraction is the important quantity deciding, if the interface is visible or not. The higher the contrast, i.e. the higher the difference between the two indices of refraction, the higher is the contribution of this interface to the reflectivity curve.

The contrast achievable decides, which probe is useful to investigate a certain structure. Fig. 9 gives an impression of the scattering lengths of different elements for neutrons and x-rays. The scattering length density, which is proportional to the dispersion δ as well for neutrons as for x-rays, is proportional to the density and to the scattering length of the elements contained in the respective layer. For x-rays, the scattering length is generally proportional to the number of electrons, while for neutrons it is quite randomly distributed over the periodic system and over the different isotopes of each element. Light atoms as well as neighbouring atoms in the periodic system cannot be distinguished well with x-rays.

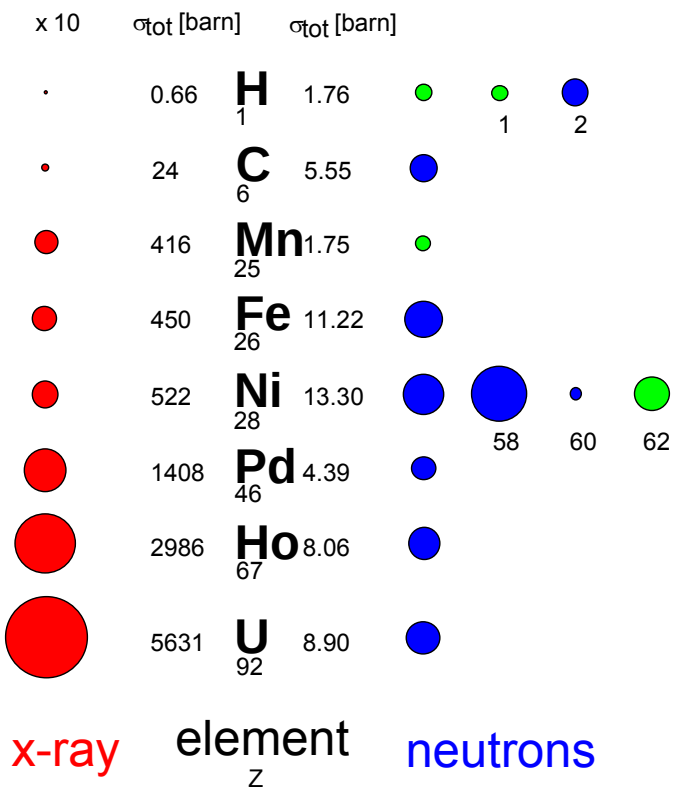

Fig. 9: *Comparison of the coherent scattering cross-sections for x-rays and neutrons for a selection of elements. The area of the circles represents the scattering cross section (x 10 for x-rays). For neutrons, the green and blue coloured circles distinguish between attractive (green, negative scattering length) and repulsive interaction (blue, positive scattering length).*

As neutrons interact strongly with the magnetic environment, polarized neutrons also show a contrast between layers with different magnetization (see section 6).

In case of low contrast, there might be a chance to enhance the contrast by contrast variation. In the case of neutrons, isotopic substitution is a good way to improve the contrast. Especially for two polymer layers, the contrast can be enhanced substantially by deuteration of one of the polymers, because the scattering lengths of Hydrogen ^{1}H and Deuterium ^{2}H differ strongly from each other (see the example in section 5.2). In the case of x-rays, one can modify the contrast for one element by tuning the x-ray energy to a resonance. An example is shown in section 5.3.

5 Layers and interfaces: Specular reflectivity of neutrons and x-rays

5.1 Neutron Reflectivity from a single Ni layer on glass

The first example is a neutron reflectivity measurement from a glass plate coated with a Ni layer. Such Ni coated glass plates are used in the neutron guides at several research reactors to guide cold neutron beams from the reactor to the instruments without losses. Fig. 10 shows the reflectivity curve together with a fit and several simulations.

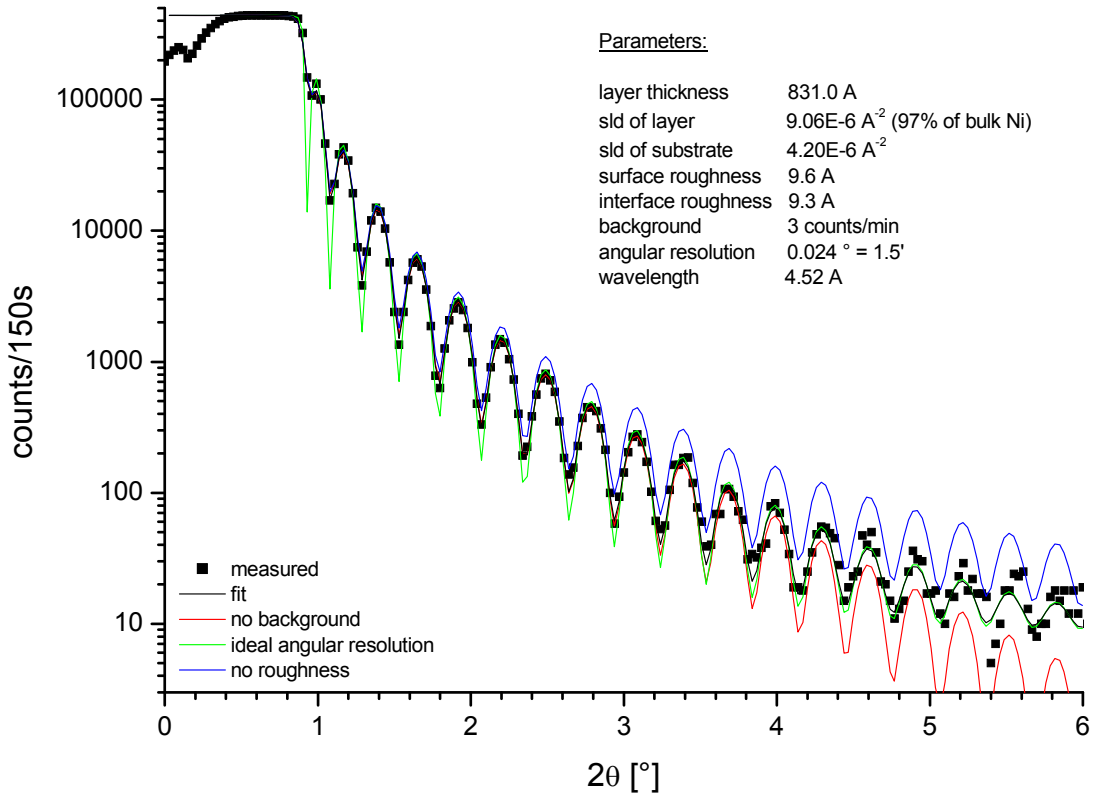

Fig. 10: *Specular reflectivity of neutrons from a Ni layer on a glass substrate, as measured with the HADAS reflectometer at the research reactor DIDO in Jülich. The black line shows the best fit, the coloured lines show simulations obtained by ignoring several parameters.*

Despite the experimental artefacts below $2\theta = 0.4°$, where the sample does not yet cover the entire beam, a typical reflectivity curve of a single layer has been measured. Up to the critical angle of $2\theta_c = 0.93°$, all impinging neutrons are reflected. At higher angles, the interference fringes of the reflections at the surface and at the interface are clearly visible. As the reflectivity drops quickly above the critical angle, it is plotted on a logarithmic scale.

It can be seen that the fit takes into account 8 parameters; some of them describe the experimental setup and some of them the sample's properties. The main parameters from the experimental setup are the wavelength used, the angular resolution of the incoming beam and the background. In the simulation of the green curve, where the resolution has not been taken into account, one can see the minima much more distinct than in the measurement. Due to the limited resolution in the real experiment, the minima are washed out due to the higher reflectivity of neutrons impinging under slightly different angles. The red curve, where the background has been omitted, shows that the signal-to-noise ratio of the instrument is strongly limited by the background, because the incoming intensity is small compared to a x-ray beamline.

The main physical parameters of the sample that have been derived from the measurement are the scattering length densities of the layer and the substrate, the roughnesses of surface and interface and, of course, the layer thickness.

The layer thickness is the easiest, it can be estimated by the distance between the maxima. The highest scattering length density (in this case of the layer) determines the critical angle θ_c, while the difference of the scattering length densities determines the height of the fringes. From the knowledge, that the layer consists of natural Ni, we have been able to determine that the density of the layer is only 97% of the bulk density, i.e. during the sputtering process a small fraction of voids has been introduced into the layer. The information about the density and the composition are not independent! Only one of the two can be derived from the reflectivity measurement.

The effect of the roughness is a drop of the reflectivity curve at high angles. The blue curve shows a simulation of the reflectivity of perfectly flat surface and interface. The growing uncertainty of the path length between two rough interfaces with growing angle of incidence leads to a decrease of interference quality with higher angles and therefore to a drop in reflectivity.

5.2 Segregation of polymer mixture under annealing

The second example shows a structure of polymer layers, where a chemical reaction at the interface between the two polymers takes place [8]. To increase the sticking between two layers of immiscible polymers, some polymer chains have a functional group ("telechelic") added which finds reaction partners in the other layer to form a multiblock copolymer (see Fig. 11). This multiblock copolymer is then fixed to the interface, with some sections compatible to polymer A and some sections compatible to polymer B.

The chemical reaction changes the sample only at the buried interface, no sign of the modification of the system is present at the surface.

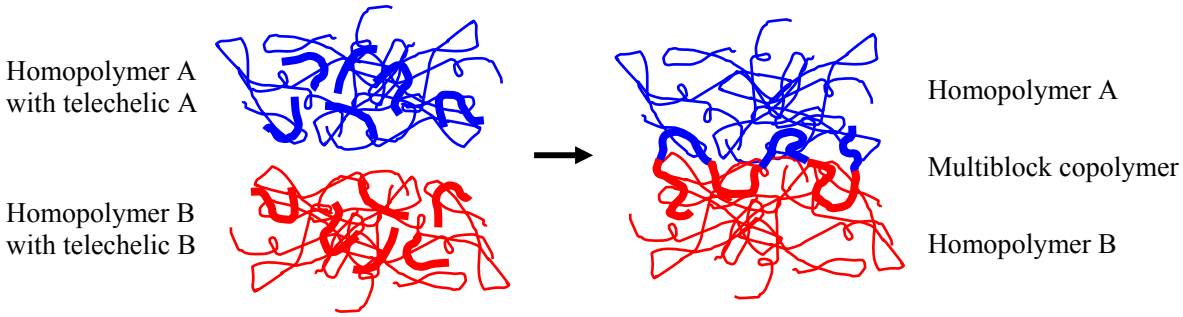

Fig. 11: *A schematic of the in situ interfacial reaction of telechelic oligomers in an immiscible polymer blend resulting in the formation of multiblock copolymer*

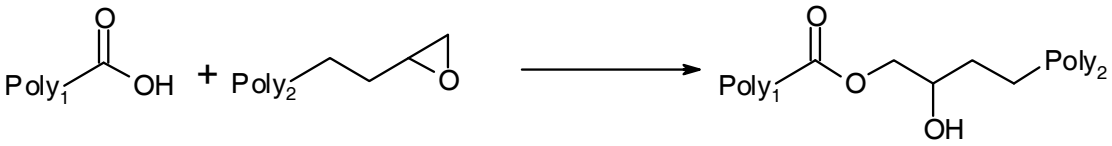

Fig. 12: *A schematic of the reaction that takes place between the carboxylic acid and epoxy groups that were present on the reactive polymer chain ends*

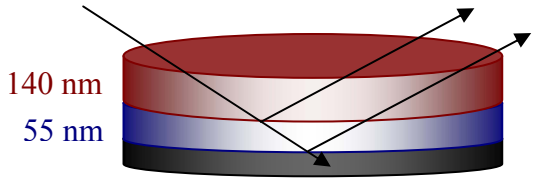

PS/dPS diepoxy telechelic (10%)
PMMA/PMMA-COOH (50%)
Silicon

Fig. 13: *Sample used for the neutron reflectivity experiment.*

Fig. 13 shows the sample used for this investigation. The bottom layer consists of poly methyl methacrylate (PMMA) and PMMA with a carboxylic acid group at the end. The top layer consists of polystyrene (PS) and deuterated PS with epoxy functional groups. The mobility of the polymer chains at room temperature is low, so that only the molecules react with each other that meet by chance at the interface. The reaction scheme is shown in Fig. 12. During annealing in vacuum at 150°C the mobility is increased strongly, so that more reactive groups diffuse towards the interface, where they react and become immobile.

The strong contrast between the deuterated functionalized PS and all other polymers with natural hydrogen makes the enrichment of the reactive polymer at the interface clearly observable.

Fig. 14 shows the neutron reflectivity data measured on the virgin sample as well as after several annealing steps. It can be seen that the shortest period hardly changes but the modulation of the peak height changes drastically during annealing. The analysis of the data resulted in the scattering length density profile shown in Fig. 15.

The main effect during the first 15 min annealing is a sharpening of the PS/PMMA interface and a slight increase in the density of both polymers. At the same time, the total thickness of the sample is slightly reduced. This leads to the interpretation that voids in the layers have been filled. After the following annealing steps the formation of the interface layer with a high concentration of the reactive compound can be observed due to the high scattering length density of dPS. At the same time, the remaining PS layer is depleted from dPS, so that the scattering length density of this part is reduced.

From the integrated area of dPS peak of the scattering length density profile, the amount of immobilized copolymer could be derived and compared to calculations of the diffusion velocity in the polymer melt. It was shown that the kinetics of this reaction does not match the predictions of a purely diffusion-based theory.

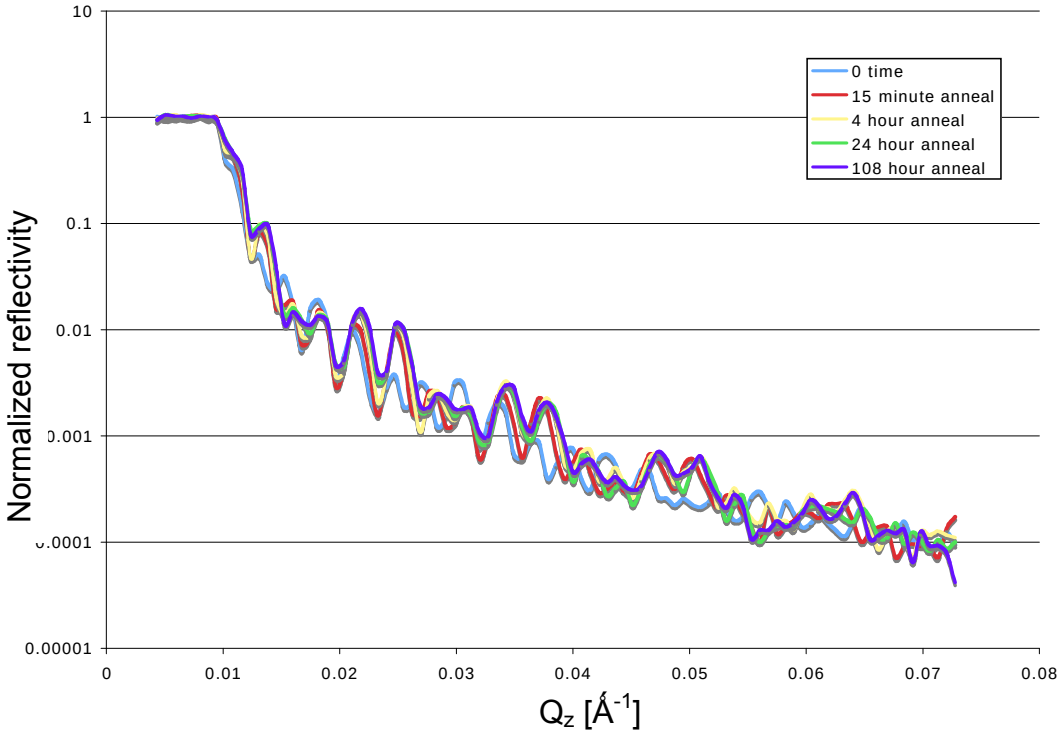

Fig. 14: *Neutron reflectivity fits from the sample shown in Fig. 13 as cast (light blue) and after 15 min, 4 hours, 24 hours and 108 hours annealing at 150 °C.*

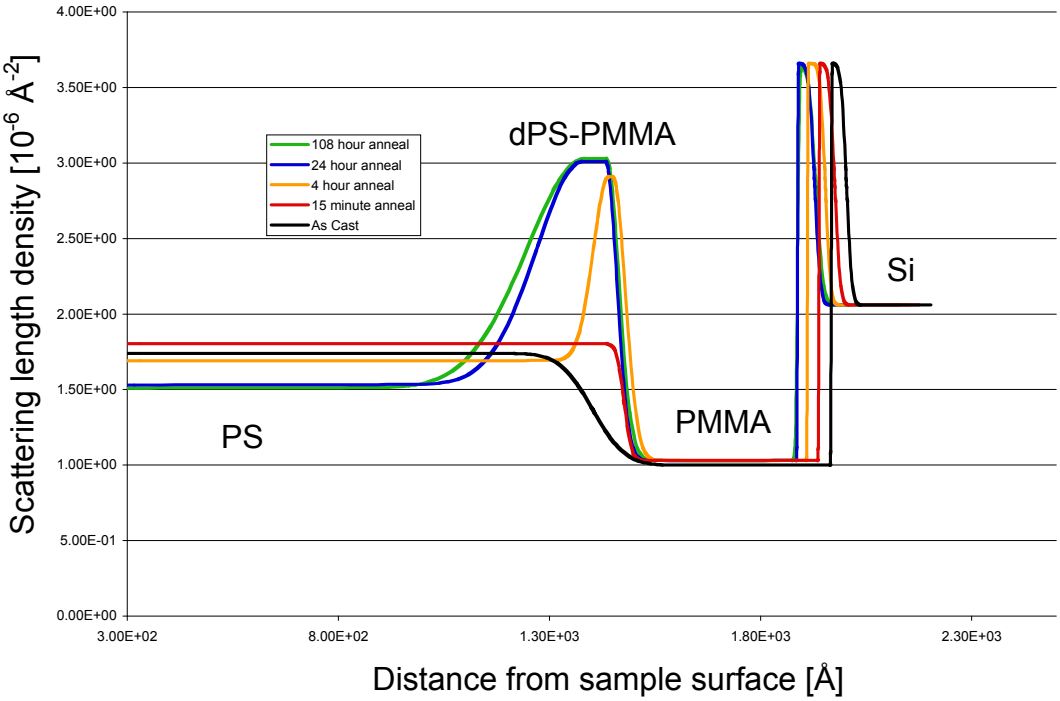

Fig. 15: *Scattering length density profile received from fitting the reflectivity data shown in Fig. 14. The sample surface is at distance 0, the Si substrate is continued towards larger distances. The colours indicate the same annealing steps as in Fig. 14*

5.3 Fe/Cr trilayer: Contrast variation with x-rays

Here, I show measurements of the buried interfaces of an epitaxially grown Fe / Cr / Fe trilayer structure on a thick Ag buffer layer. The thickness of the Ag buffer, the absorption of the x-rays over this thickness and the big roughness at the interface between Ag and the real substrate GaAs together are sufficient to be able to treat the Ag layer as substrate and to ignore everything below. The goal of this investigation is to extract information about the interface morphology of the Fe / Cr interfaces [9]. As the interface region is thin, we need to be able to measure a large Q-range, which is not possible with neutrons today. Furthermore, the influence of the magnetism in the Fe layers would have disturbed a neutron measurement.

With x-rays, we face the problem that Fe and Cr are next-nearest neighbours in the periodic system of the elements, so that the contrast for normal x-rays is very weak. The way out is anomalous x-ray scattering at a synchrotron x-ray source, where the scattering length density can be varied by choosing a x-ray energy close to the absorption edge of one of the elements.

Fig. 16 shows the dependence of the dispersion on the x-ray energy for Fe and Cr. These values have been calculated using the calculus of Cromer and Liberman [10]. It shows a strong enhancement of the contrast at the K-absorption edge of Cr, E=5989 eV and at the Fe K-edge at E=7112 eV. Unfortunately the calculation is done for free atoms and not for solids. In solids the final states are altered due to the bandstructure and the lattice, so that the dispersion calculation is not reliable over 50-100 eV above the absorption edge. Therefore, we used an energy slightly below the Cr K-edge for high contrast at the Fe / Cr interface.

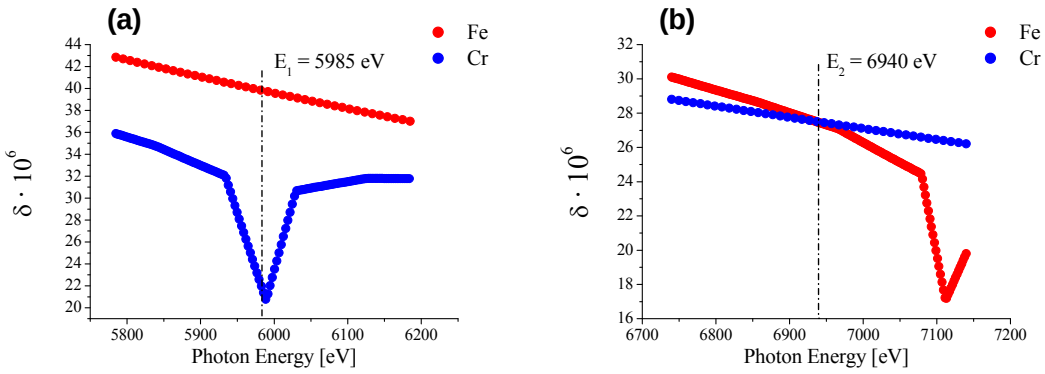

Fig. 16: *Calculated X-ray dispersion close to the Cr K-absorption edge (a) and close to the Fe K-edge (b)*

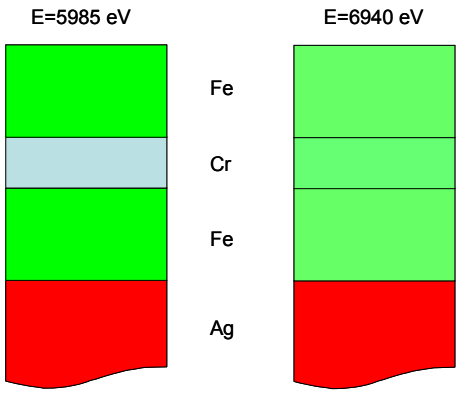

Fig. 17: *Colour schematic of the contrast in the Fe / Cr / Fe / Ag system at highest and lowest contrast*

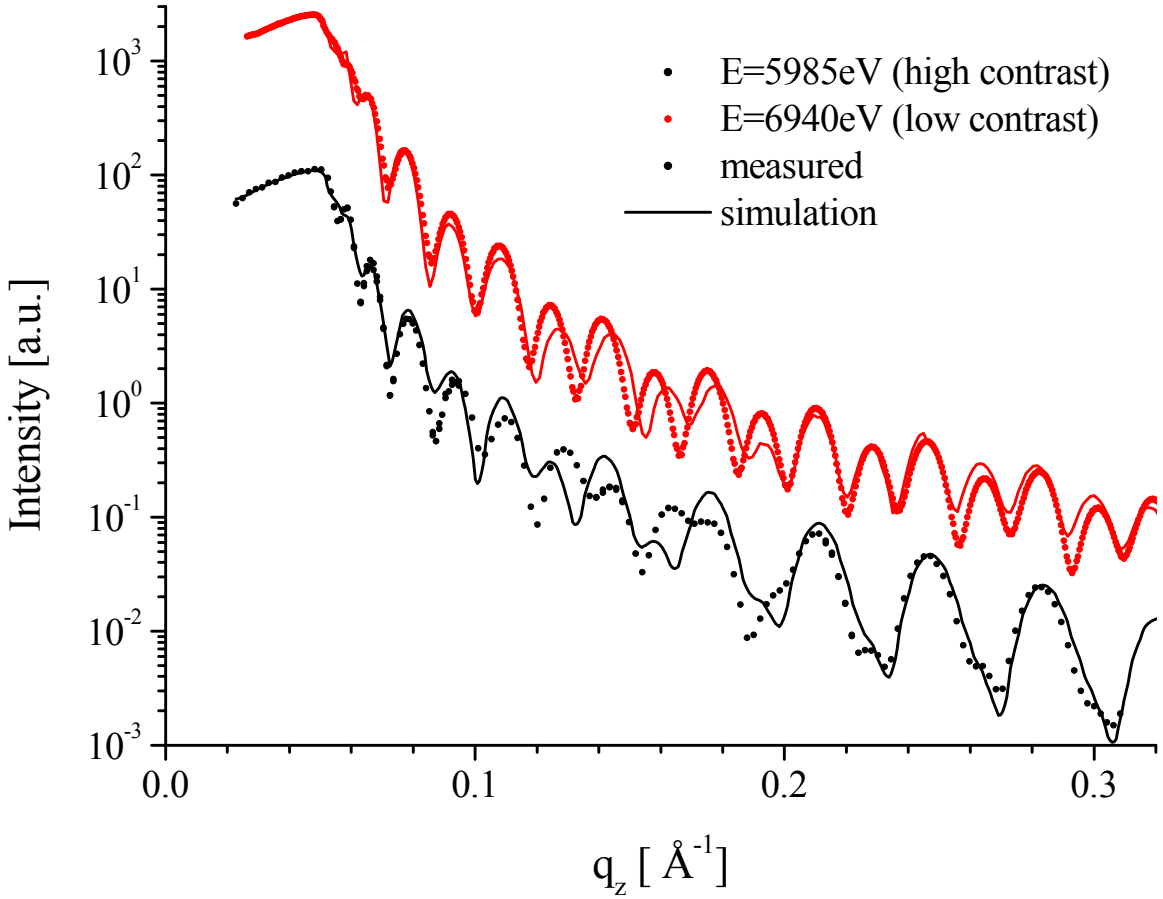

Fig. 18: *Specular reflectivity of the Fe / Cr / Fe / Ag layered structure at the two different energies with high and vanishing contrast between Fe and Cr*

At E=6940 eV, the dispersion curves for Fe and Cr cross when approaching the Fe K-edge. The contrast is vanishing. Fig. 17 shows a colour schematic of the contrasts at the two energies chosen. At 6940 eV there is no contrast at the Fe / Cr interfaces, the x-rays are reflected only at the surface and the Fe / Ag interface. The data is shown in Fig. 18. The period of the reflectivity fringes is associated with the total thickness of the Fe / Cr / Fe stack. The imperfection of the fit at about $q_z = 0.13$ Å^{-1} is due to the oxide layer on top, which is not perfectly described by the model used. The measurement at this energy can be used to fix the parameters of those interfaces which are less interesting.

At E=5985 eV, there is a strong contrast between Fe and Cr, but it is still weaker than the contrast at the surface and the contrast against the Ag substrate. The reflectivity curve is now dominated by fringes with the period according to the bilayer thickness Fe / Cr. This measurement can give reliable information about the roughness of the interface between Fe and Cr.

6 Magnetization depth profiles: Specular reflectivity of polarized neutrons

In this chapter, I would like to have a closer look at the investigation of the magnetization depth profile in magnetic layered structures. Polarized neutrons are a suitable probe for the layers' magnetization, because the neutron is a spin ½ particle and therefore interacts with the magnetic induction **B**. As reflectometry measurements average over the atomic structure of the sample, antiferromagnetic structures are not accessible due to the vanishing net magnetization. In contrast to that, magnetization densities of ferromagnetic layers can be measured on an absolute scale with reflectometry of polarized neutrons.

6.1 Index of refraction of magnetized material for polarized neutrons

We stay in the approximation of homogeneous layers with flat interfaces, where the potential for the neutron only depends on the z coordinate. In the case of magnetic multilayers, we need to take into account the interaction of the neutron's spin with the magnetic induction inside matter. To treat this properly, we have to work with wave functions in the 2-dimensional quantum mechanical spin space, where the usual space-dependent functions, e.g. the potential, become operators on the neutron's spin.

The potential for the interaction of the neutron with matter in the layer l can be separated into two parts

$$\hat{V}_l = V_l^N \hat{1} + \hat{V}_l^M \tag{25}$$

where V_l^N is the nuclear interaction from eq. (3), $\hat{1}$ is the unity operator, which does not affect the spin state, and $\hat{V}_l^M = -\mu_n \hat{\boldsymbol{\sigma}} \cdot \mathbf{B}_l$ is the magnetic dipole interaction operator between the neutron magnetic moment operator $\mu_n \hat{\boldsymbol{\sigma}}$ and the magnetic induction $\mathbf{B}_l$.

We assume the direction of the external magnetic field $\mathbf{H}=H\mathbf{e}_x$ to be oriented in the x-direction of the coordinate system defined in Fig. 5. Then it is convenient to choose also the x-axis as quantization axis for the neutron spin, so that the order of the Pauli matrices in the spin operator $\hat{\boldsymbol{\sigma}} = (\sigma_x, \sigma_y, \sigma_z)$ is the following.

$$\sigma_x = \begin{pmatrix} 1 & 0 \\ 0 & -1 \end{pmatrix} \qquad \sigma_y = \begin{pmatrix} 0 & 1 \\ 1 & 0 \end{pmatrix} \qquad \sigma_z = \begin{pmatrix} 0 & -i \\ i & 0 \end{pmatrix} \tag{26}$$

It is arbitrary to choose the coordinate system for the scattering experiment (Fig. 5) and for the neutron spin to be parallel; the result does not change, if the magnetic field **H**, which defines the quantization axis for the spin, is rotated to any other direction in the x-y-plane of the scattering experiment. This rotation will only change the phase of the spin-flip scattering (eq. 30), which has no influence on the reflectivities and transmissivities.

The magnetic induction can be decomposed into terms of applied field and magnetization

$$\mathbf{B} = \mu_0(\mathrm{H}\mathbf{e}_x + (1-\mathrm{D})\mathbf{M}) = \mathbf{B}_0 + \mu_0(1-\mathrm{D})\mathbf{M} \tag{27}$$

where $\mathbf{B}_0$ is the induction from the external magnetic field, D is the demagnetizing factor and $\mathbf{M}$ the magnetization of the material. In the case of a thin film, (1 – D)$\mathbf{M}$ is equal to the in-plane component of the magnetization.

The magnetization component M_z perpendicular to the film surface cannot induce any magnetic contrast between adjacent layers, because $\nabla \cdot \mathbf{B} = 0$ does not allow B_z to change discontinuously when crossing an interface. In fact, this is the origin of the demagnetizing effect.

$\mathbf{B}_0$ is constant over the sample volume and therefore gives a constant contribution to the index of refraction as well for vacuum as for every material involved. Therefore, all these contributions cancel out when calculating reflectivity R and transmissivity T according to (18) and (19).

The only remaining contributions are M_x parallel to the quantization axis and M_y perpendicular to the quantization axis, but in plane. With that, we can rewrite the total interaction operator in analogy to (5) as

$$\hat{\mathrm{V}}_l = \frac{2\pi\hbar^2}{\mathrm{m}}(\rho_l^{\mathrm{N}}\hat{1} + \rho_l^{\mathrm{M}}\hat{\boldsymbol{\sigma}} \cdot \mathbf{b}_l) \tag{28}$$

with the nuclear scattering length density ρ_l^{N}, the magnetic scattering length density ρ_l^{M} and the unit vector $\mathbf{b}_l$ along the magnetic induction vector $\mathbf{B}_l$ in layer l. In most cases, if $\mu_0 M >> B_0$, $\mathbf{b}_l$ is approximately parallel to $\mathbf{m}_l$.

In complete analogy to section 4, the Schrödinger equation can be solved in coordinate and spin space. The eigenvectors $|+\rangle$ and $|-\rangle$ of the operator $\hat{\boldsymbol{\sigma}} \cdot \mathbf{b}_0 = \sigma_x$ with the eigenvalues +1 and -1, respectively, define states of the neutron with “spin up” and “spin down”. The solution of the Schrödinger equation is the neutron state $|\Psi(\mathbf{r})\rangle$, which is again a linear combination of those two eigenvectors:

$$|\Psi(\mathbf{r})\rangle = \Psi^+(\mathbf{r})|+\rangle + \Psi^-(\mathbf{r})|-\rangle = \begin{pmatrix} \Psi^+(\mathbf{r}) \\ \Psi^-(\mathbf{r}) \end{pmatrix} \tag{29}$$

We end up with a set of two coupled one-dimensional linear differential equations for every layer:

$$\begin{aligned}\Psi_l^{+\,\prime\prime}(z)+\left[k_{zl}^2-4\pi(\rho_l^N+\rho_l^M m_{xl})\right]\Psi_l^+(z)-4\pi\rho_l^M m_{yl}\Psi_l^-(z)=0\\ \Psi_l^{-\,\prime\prime}(z)+\left[k_{zl}^2-4\pi(\rho_l^N-\rho_l^M m_{xl})\right]\Psi_l^-(z)-4\pi\rho_l^M m_{yl}\Psi_l^+(z)=0\end{aligned} \tag{30}$$

The solution of this set of differential equations can be done in analogy to (23). The calculation is straightforward, but lengthy. Its solution can be found in [11]. It ends with the reflection and transmission operators $\hat{r}_l$ and $\hat{t}_l$, which are again operators in spin space with two different eigenvalues.

Four types of reflectivities can be measured, which are the squares of the projections of the reflection amplitude onto spin up or down neutron states:

$$R^{\pm\pm}=\left|\langle\pm|\hat{r}_0|\pm\rangle\right|^2 \tag{31}$$

These reflectivities have a clear physical meaning. From eq. (30) it is clear that only nuclear scattering and the magnetization component M_x parallel to the field lead to non-spinflip (NSF) reflectivities. By analysis of the sum and the difference of R^{++} and R^{--}, these two contributions can be separated from each other. Fig. 19 shows the influence of the magnetic scattering length density on the critical angle and the Reflectivity for the case of a magnetically saturated surface, where only NSF reflectivity is present.

The spin-flip (SF) reflectivities R^{+-} and R^{-+} are equal to each other and arise from the magnetization component M_y in plane, perpendicular to the field. As the sign of the magnetization is only coded in the phase of the SF reflected wave, it is lost when measuring the intensities. Therefore, only $|M_y|$ can be measured.

In conclusion, polarized neutron reflectivity can measure the nuclear scattering length density ρ^N and the magnetization components M_x and $|M_y|$ for every layer in the thin film structure.

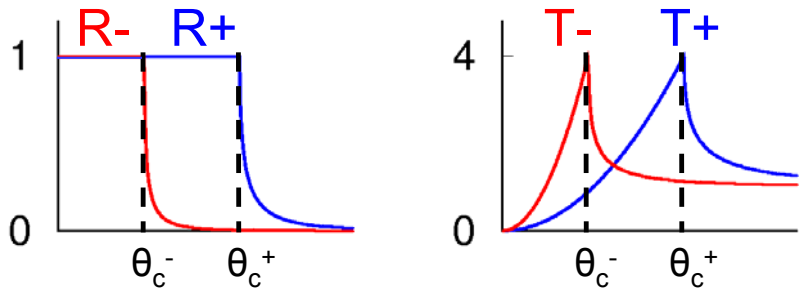

Fig. 19: *Reflectivity and Transmissivity for polarized neutrons from a saturated ferromagnetic material*

6.2 Magnetic contrast: Co/Cu multilayer

This example shows experimentally the contrast for polarized neutrons which depends as well on the nuclear as on the magnetic scattering length densities. We have measured the reflectivity of a multilayer with 20 periods of a Co layer and a Cu layer [12]. The thickness of the Cu layer is so that the Co layers are coupled ferromagnetically, and the sample has been saturated in a strong magnetic field. During the experiment, the guiding field, which defines the quantization axis for the neutron spin, is kept parallel to the magnetization of the Co layers.

The nuclear scattering length density for Co is 2.3 E-6 $Å^{-2}$. For Cu it is much higher 6.53 E-6 $Å^{-2}$. The magnetic scattering length density for Co is 4.24 E-6 $Å^{-2}$. So the sum of nuclear and magnetic scattering length density of Co hardly differs from the scattering length density of the non-magnetic Cu, so that there is no contrast for spin-up neutrons, i.e. neutrons with the spin parallel to the external field. The contrast for spin-down neutrons, which feel the difference of nuclear and magnetic scattering length density, is huge. Fig. 20 shows a colour sketch of the different contrasts.

Fig. 21 shows the reflectivity curve for spin-up and spin-down neutrons. As no magnetization component perpendicular to the field is present, the spin-flip channels only contain a signal coming from the imperfect polarisation of the beam and are not shown. The total reflection angle for both channels is the same because it is dominated by Cu. Due to the large contrast for spin-down neutrons, two Bragg peaks at $2\theta=3°$ and at $2\theta=6°$ corresponding to the structural periodicity are easily observed already after short beam time. The reflectivity curve for spin-up neutrons is rather unstructured due to the missing contrast between magnetized Co and Cu.

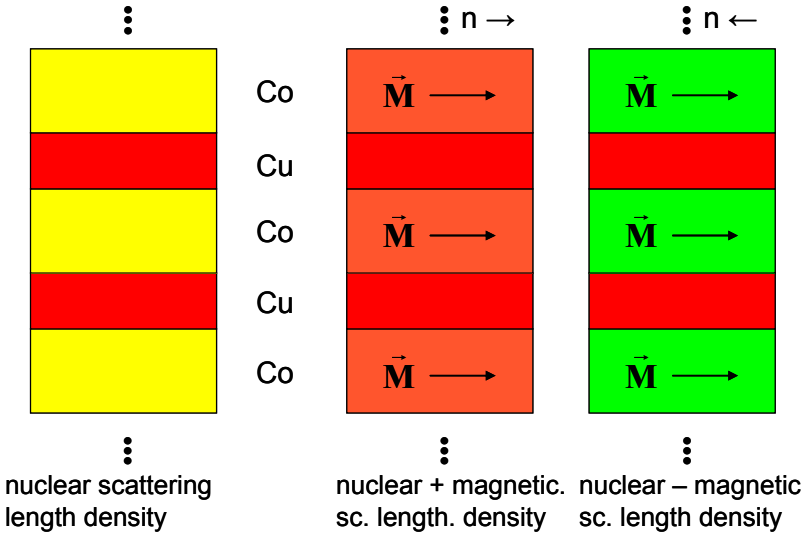

Fig. 20: *Colour representation of the contrasts in a magnetically saturated Co / Cu multilayer. Purely nuclear contrast (left), contrast for spin up neutrons (middle) and contrast for spin down neutrons (right)*

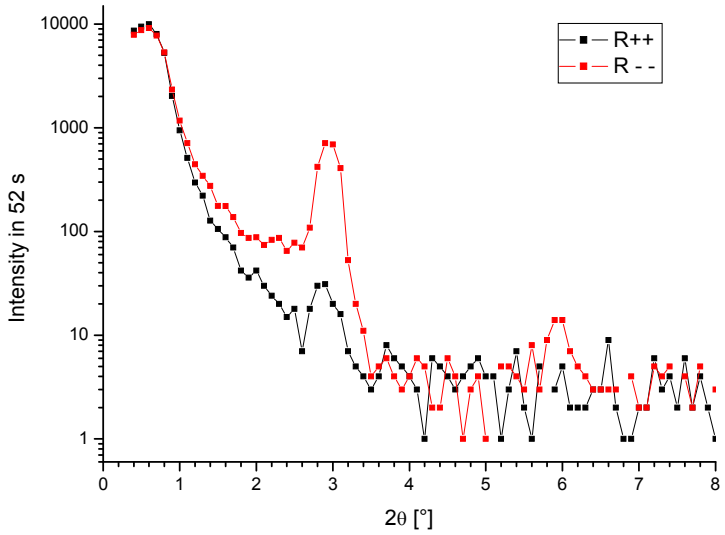

Fig. 21: *Specular reflectivity of polarized neutrons from a magnetically saturated Co/Cu multilayer. For spin-down neutrons two Bragg peaks at 2θ=3° and 6° are clearly visible while the reflectivity curve for spin-up neutrons is hardly structured.*

6.3 Layer-by-layer magnetometry: Polarizing supermirror

Polarizing supermirrors are commonly used for the polarization of cold neutron beams. For the operation of a polarized neutron instrument, it is of course important to know the performance of the polarizers used and their behaviour in the magnetic field. During the characterization of the device, it turned out that a lot of physics of the layered magnetic structure can be understood by having a closer look at the data, and so we have investigated the polarizing supermirror thoroughly [13,14]. In this section, I will present the laterally averaged data from specular reflectivity; the off-specular and GISANS measurements can be found in reference [14].

A polarizing supermirror is a stack of bilayers of a magnetic and a non-magnetic material. The thickness of the bilayers is gradually increasing to receive constructive interference for a broad range of Q-values, what results in an extended plateau of high reflectivity above the total reflection angle. The materials are chosen to have a high contrast for one spin direction and no contast for the other.

The supermirror we have investigated is a polarizing supermirror produced by Swissneutronics which reflects the neutrons with the proper spin direction up to m=2.5 times the critical angle of Ni. The first three columns of Fig. 22 show the intended scattering length density sequence. 100 bilayers of FeCoV (ferromagnetic) and TiN (nonmagnetic) with gradually increasing thickness are transparent for neutrons with spin antiparallel to the

magnetization and reflecting for neutrons with spin parallel to the magnetization. Below the stack, there is a strongly absorbing Gd layer to absorb all spin down neutrons and a glass substrate for mechanical stability.

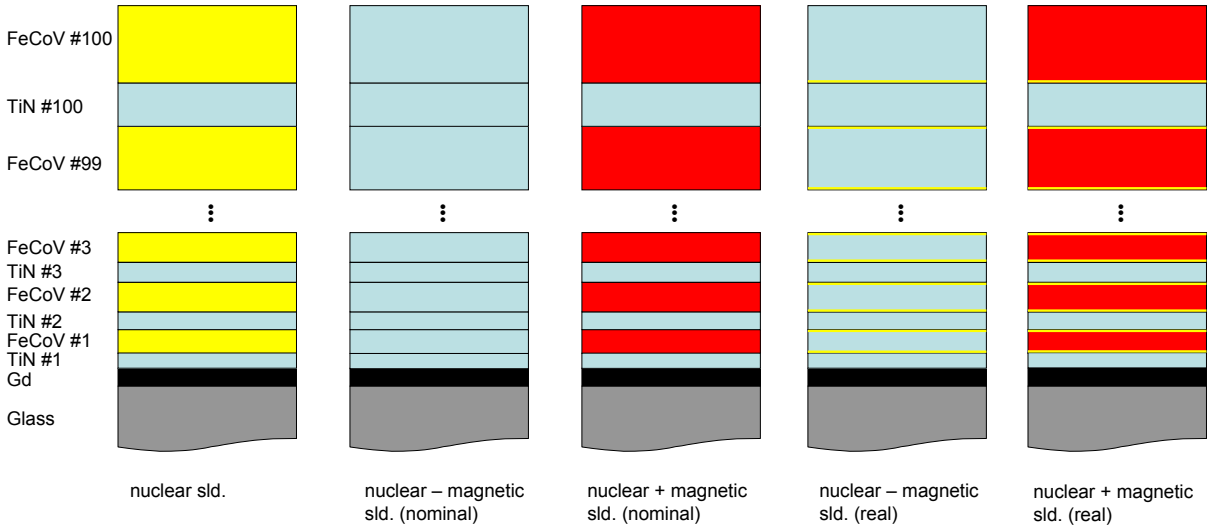

Fig. 22: *Colour representation of the scattering length density distribution in a polarizing supermirror. On the left, the nuclear scattering length density distribution is shown. The next two columns show the intended contrast for neutrons with spin antiparallel to the magnetization (no contrast) and for neutrons with spin parallel to the magnetization (high contrast). The two columns on the right show the measured scattering length density profile. We found magnetically dead layers at the interfaces between FeCoV and TiN, so that a 2-4Å of the FeCoV layer show only the nuclear scattering length density, but no magnetic contribution.*

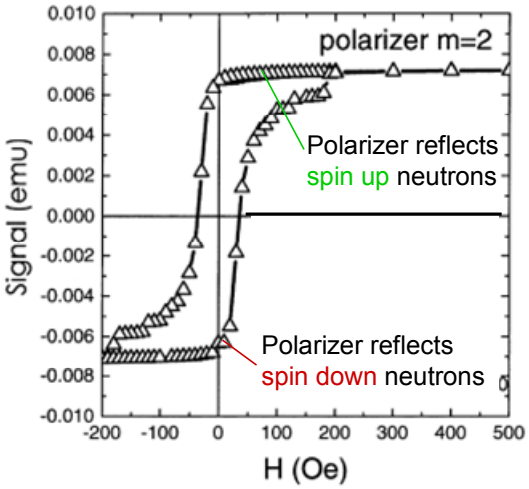

Fig. 23: *Magnetization curve of a polarizing supermirror with 40 bilayers [15]*

As our sample cannot be measured in a magnetometer because the back surface is also coated magnetically, we show the magnetization curve of a comparable sample with only 40 bilayers in Fig. 23. After negative saturation, the polarizer remains almost completely saturated in negative direction at small positive fields. This allows two different working conditions for the polarizer. On the one hand, it can work in saturation, i.e. after exposure to a high positive magnetic field. Then all magnetic layers are magnetized along the field direction, and the supermirror reflects spin-up neutrons, i.e. neutrons with spin along the magnetic field. On the other hand, it can be used in remanence with all layers magnetized opposite to the applied (small) magnetic field. Then the spin-down neutrons are reflected.

Fig. 24 shows the polarized neutron reflectivity measurement at different fields after negative saturation. Fig. 24 a) shows the remanence. In the "working range" up to α_i = 21 mrad, the reflectivity for spin down neutrons R^{--} is more than two orders of magnitude higher than R^{++}, yielding a good negative polarization of the reflected beam. The reflectivity for the proper polarization channel is close to 1, the increasing slope at small angles is an experimental artefact due to the increasing coverage of the beam's cross section with increasing angle of incidence. The spin-flip signal is completely determined by the imperfect polarization of the incident beam, no spin-flip specular reflectivity is coming from the sample. Fig. 24 d) is measured at saturation and is almost exactly opposite to the remanent state.

In the two intermediate states shown in Fig. 24 b) and c), there is a crossover between R^{++} and R^{--}, showing that some of the layers are magnetized along and some antiparallel to the field. In the fit, we can address the individual magnetization of every layer and find out, which layers have flipped and which stay magnetized opposite to the field direction. It turned out, that the thinner, i.e. lower magnetic layers flip first. In the case of 3.8 mT (Fig. 24 b), 48 layers have flipped, in the case of 5.6 mT (Fig. 24 c), 94 FeCoV layers have flipped in field direction. Fig. 25 shows the number of layers flipped in field direction as a function of the field strength.
What is striking, is the relatively high R^{--} signal in saturation that drops at twice the angle of the end of the supermirror plateau. It shows that spin-down neutrons see a structure that has half the period of the intended supermirror structure for the spin-up neutrons. It turned out, that this feature comes from magnetically dead layers at the interface between FeCoV and TiN. At the top and the bottom of the FeCoV layer, there is a 2 – 4 Å thick nonmagnetic region with the purely nuclear scattering length density of FeCoV. The two pictures on the right side of Fig. 22 show a schematic of the real scattering length density profile, where the reflectivity in R^{--} comes from the yellow – blue bilayers, that have about half the thickness of the red – blue bilayers that result in R^{++}.

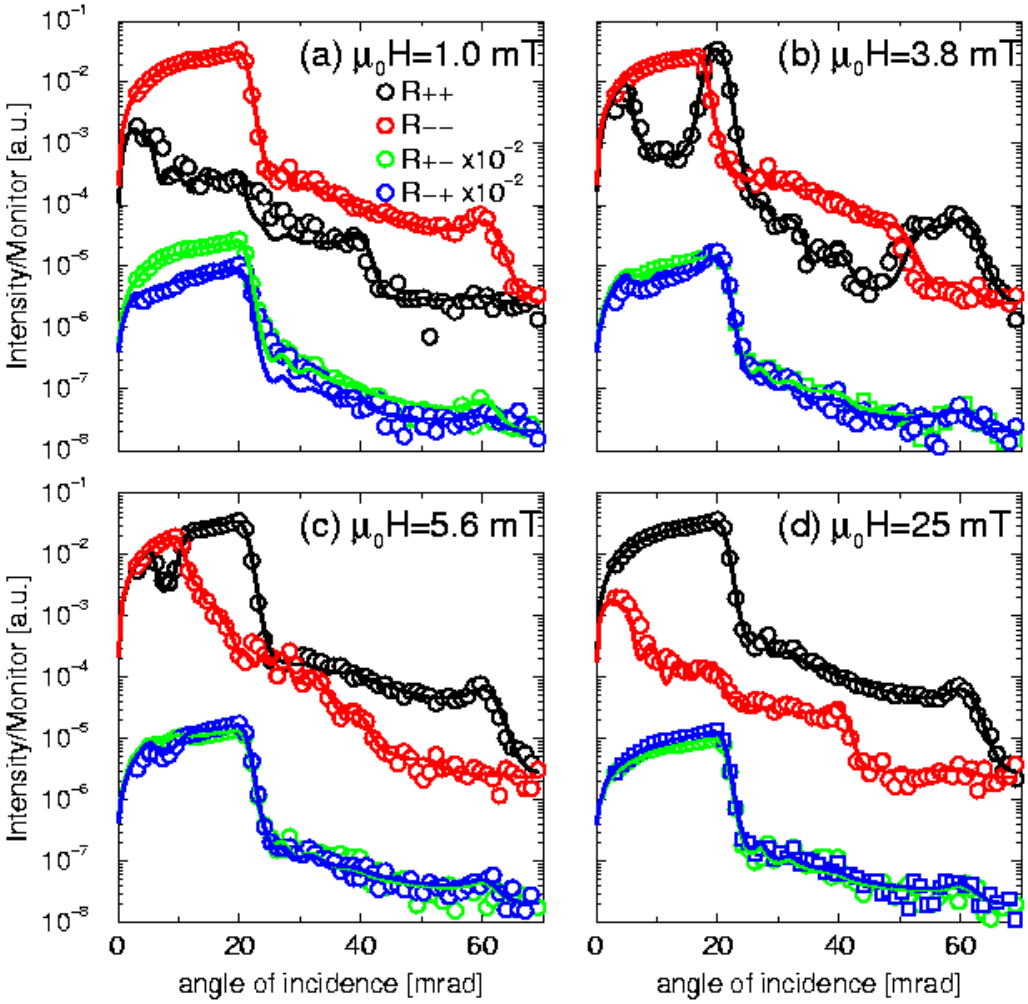

Fig. 24: *Polarized neutron reflectivity measurements on the polarizing supermirror at different magnetic fields applied after negative saturation. The dots show experimental data, the lines are fits.*

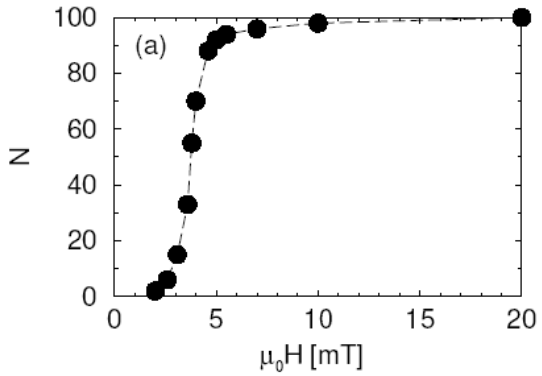

Fig. 25: *Number of FeCoV layers flipped in field direction as a function of the positive magnetic field applied after negative saturation*

7 Scattering from lateral fluctuations

7.1 Lateral correlations in layered structures

The normal case of real layered structures is that they are not completely laterally homogeneous but they show at least some roughness at the interfaces. Chemical deviations may come from interdiffusion at an interface or oxidation processes at the sample surface. Magnetic layers split laterally into magnetic domains which are visible for polarized neutrons. Lateral structuring of layered structures is of high technological importance for many applications in modern electronic devices.

If lateral fluctuations (i.e. all local variations in scattering length density from the laterally averaged scattering length density) exist with a correlation length smaller than the projected coherence lengths (eq. (2) and (3)), then scattering under grazing incidence can be observed. At grazing incidence, those coherence lengths can extend into the µm range and the interaction of the x-ray photons or neutrons with the fluctuations will lead to multiple scattering processes within this surface, so that the Born approximation will not be able to describe the effects properly.

In most cases, the layered structure is dominant, so that the main scattering feature is the specular reflection that is caused by the laterally averaged scattering length density contrasts. In this case, the potential inside layer l can be decomposed into two terms describing the laterally averaged potential (as main potential $V_l^0(z)$) and the fluctuations around the main potential $V_l^1(\mathbf{r})$.

$$V_l(\mathbf{r}) = V_l^0(z) + V_l^1(\mathbf{r}) \tag{32}$$

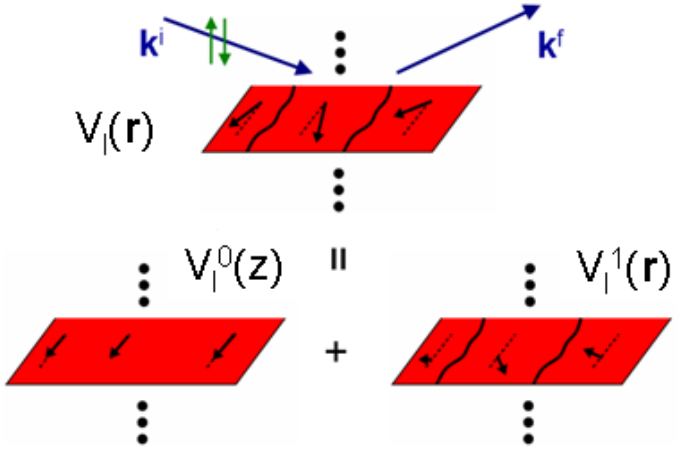

Fig. 26: *Decomposition of the potential of layer l for the treatment with the DWBA*

Fig. 26 shows the decomposition of the potential of the layer no. l in the case of magnetic domains. The main potential V^0 shows a homogeneous magnetization for every layer. It is defined by the lateral average magnetization direction and modulus. V^1 contains all deviations in magnetization direction and the domain walls.

In a comparable way, the formalism can be defined for interface roughness, interdiffusion or chemical precipitations.

The main potential then can be treated exactly (see section 4), and the fluctuations can be treated in the framework of the Distorted Wave Born Approximation (DWBA) as a perturbation. Then, all refraction effects close to θ_c and reflected wavefields are taken into account as origin of off-specular scattering. Depending on the length scale of the correlations, they can be seen in offspecular scattering (in x-direction, where the coherence length extends into the μm range) or in GISAS geometry for fluctuations in the nm scale.

A description of the DWBA formalism for the case of magnetic domains can be found in [16]. Different cross sections are used in the case for interface fluctuations or density fluctuations within layers separated by flat interfaces [17, 18, 19, 20, 21, 22]. Today, off-specular scattering from many structures can be modelled successfully. Modelling GISAS scattering is still a challenge in the framework of the DWBA, but first successful results are published for systems with a high degree of order.

7.2 Off-specular scattering from nanoparticle supercrystals

Here, I would like to present the scattering results from a system, where very different length scales are realized in a single sample. The sample consists of spherical Fe_2O_3 nanoparticles with 9.5 nm diameter surrounded by an organic ligand shell, which originally are dispersed in an organic solvent. When this solution is drop-casted onto a flat Si wafer surface and the solvent evaporates slowly, the nanoparticles self-assemble in well-ordered supercrystals with dimensions up to 2 μm in diameter and 1 μm in height. These supercrystals are then randomly spread over the wafer surface [23, 24] with a typical spacing of a few μm.

Fig. 27 shows a scanning electron microscope (SEM) picture of the arrangement of supercrystals on the surface of a Si wafer. One can see a lot of crystals which are bigger than 1 μm and spread over the surface with several μm of space in between. In between the supercrystals, some single nanoparticles remain on the Si surface, which are not ordered. When zooming in, one can see the perfect order of the nanoparticles within a single supercrystal (Fig. 28). The SEM picture gives the impression that the nanoparticle layers inside the supercrystals are parallel to the surface of the Si wafer.

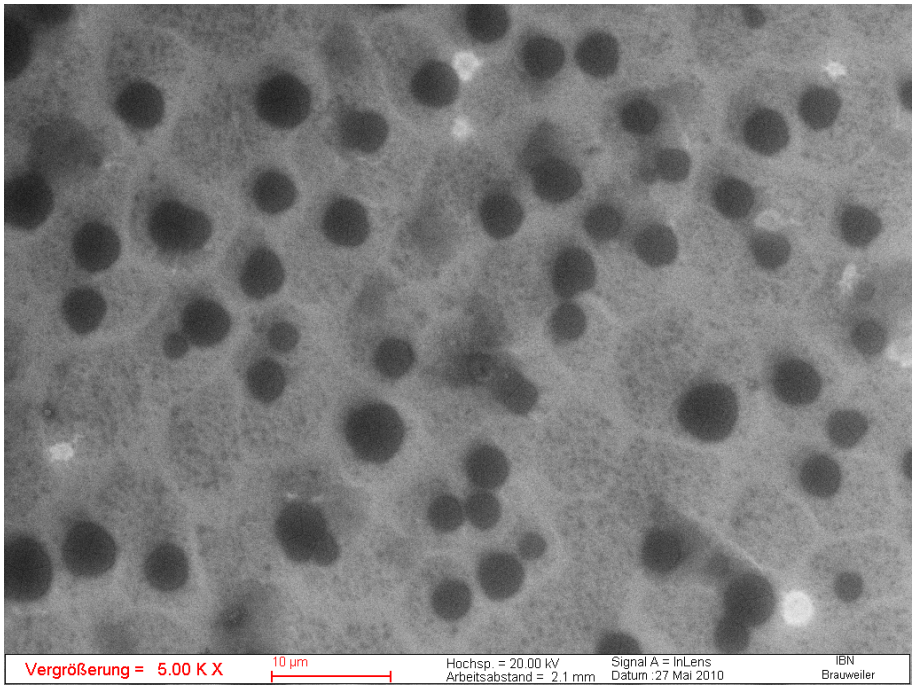

Fig. 27: *SEM (Scanning electron microscope) picture of self-organized nanoparticle supercrystals dispersed over the surface of a Si wafer.*

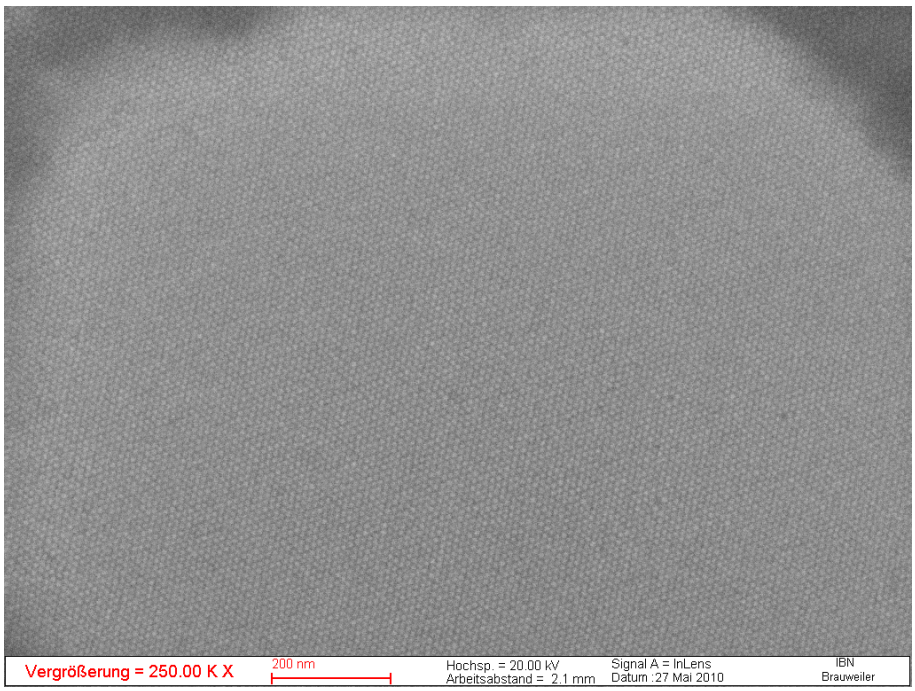

Fig. 28: *SEM picture zoomed into one supercrystal showing the perfect order of the nanoparticles on the surface of the supercrystal*

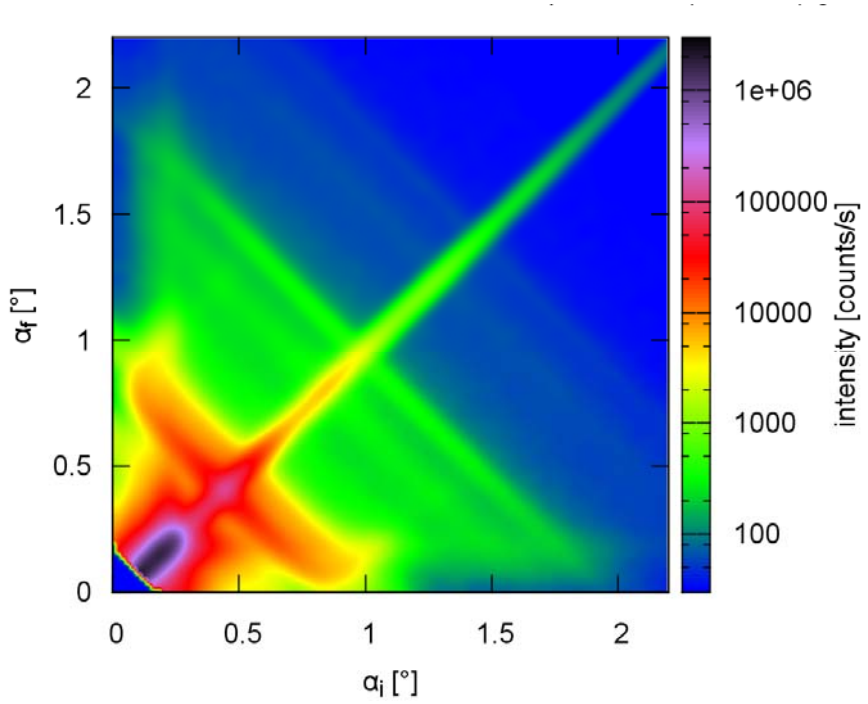

Fig. 29: *Specular reflectivity and offspecular x-ray scattering from an array of nanoparticle supercrystals. The specular reflectivity can be found in the main diagonal of the image, where* $\alpha_i = \alpha_f$.

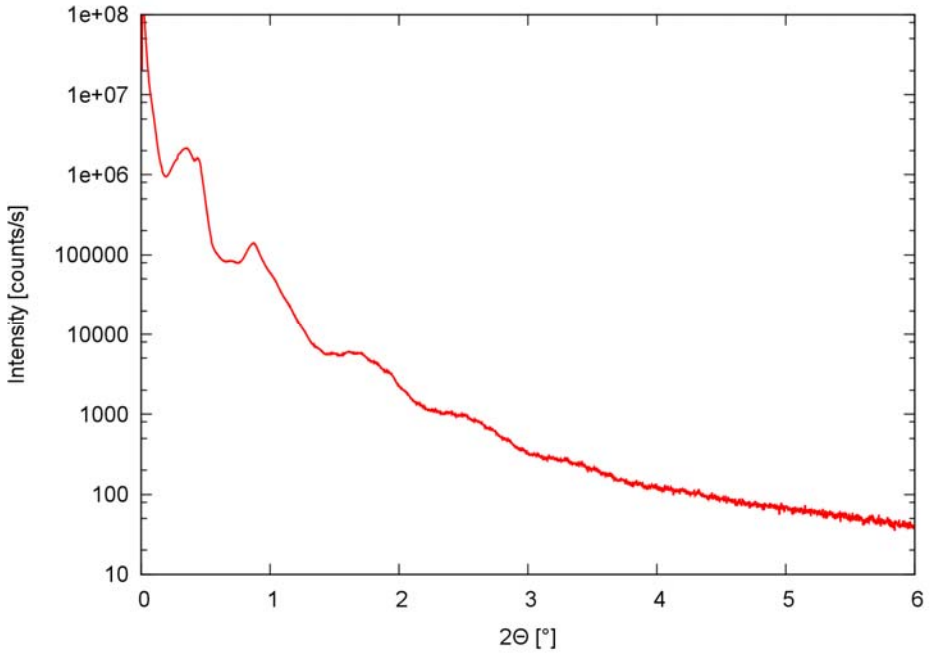

Fig. 30: *Specular reflectivity extracted form the measurement presented in Fig. 29*

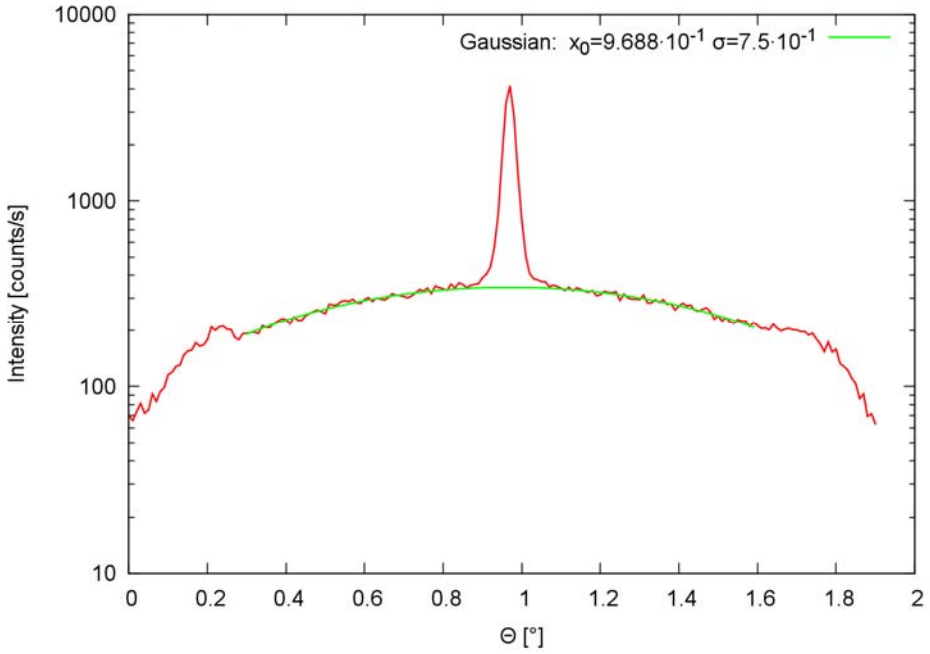

Fig. 31: *Rocking scan at* $\alpha_i + \alpha_f = 1.9°$ *out of the measurement presented in Fig. 29. In the middle, one can see the specular reflection which dominates the curve. Below the specular reflection there is offspecular scattering which can be fitted with a Gaussian describing the lateral correlations between the neighboring supercrystals. The peaks at* $\theta = 0.25°$ *and* $\theta = 1.65°$ *are due to the Yoneda effect at* $\alpha_i = \theta_c$ or $\alpha_f = \theta_c$, resp.

Fig. 29 shows the specular reflectivity and the off-specular scattering measured from the surface of such a supercrystal array with x-rays with Cu Kα wavelength (λ = 1.54 Å). One can see the specular reflectivity dominant in the main diagonal of the figure together with a lot of offspecular scattering, mainly perpendicular to the main diagonal.

The specular reflectivity, which is extracted in Fig. 30, shows clear oscillations showing a layered structure perpendicular to the sample surface. This is the first proof of the alignment of the inner structure of all (!) supercrystals with the surface of the Si wafer. The period of the oscillations reveals the layer thickness, which in this case is the thickness of a close-packed layer of nanoparticles with organic shell. Therefore, the layer thickness is slightly thicker than the nanoparticle diameter.

In offspecular scattering, one can observe many Bragg sheets perpendicular to the specular direction. These Bragg sheets arise from lateral fluctuations which are periodical in the thickness. In this case, they are the supercrystals which obviously have the same place in every layer. Close to the axes of the plot in Fig. 29 one can see that the offspecular scattering features are bent due to refraction effects. The intensity is enhanced there because of the increased wavefield along the surface close to the critical angle θ_c (Yoneda effect, cf. Fig. 8).

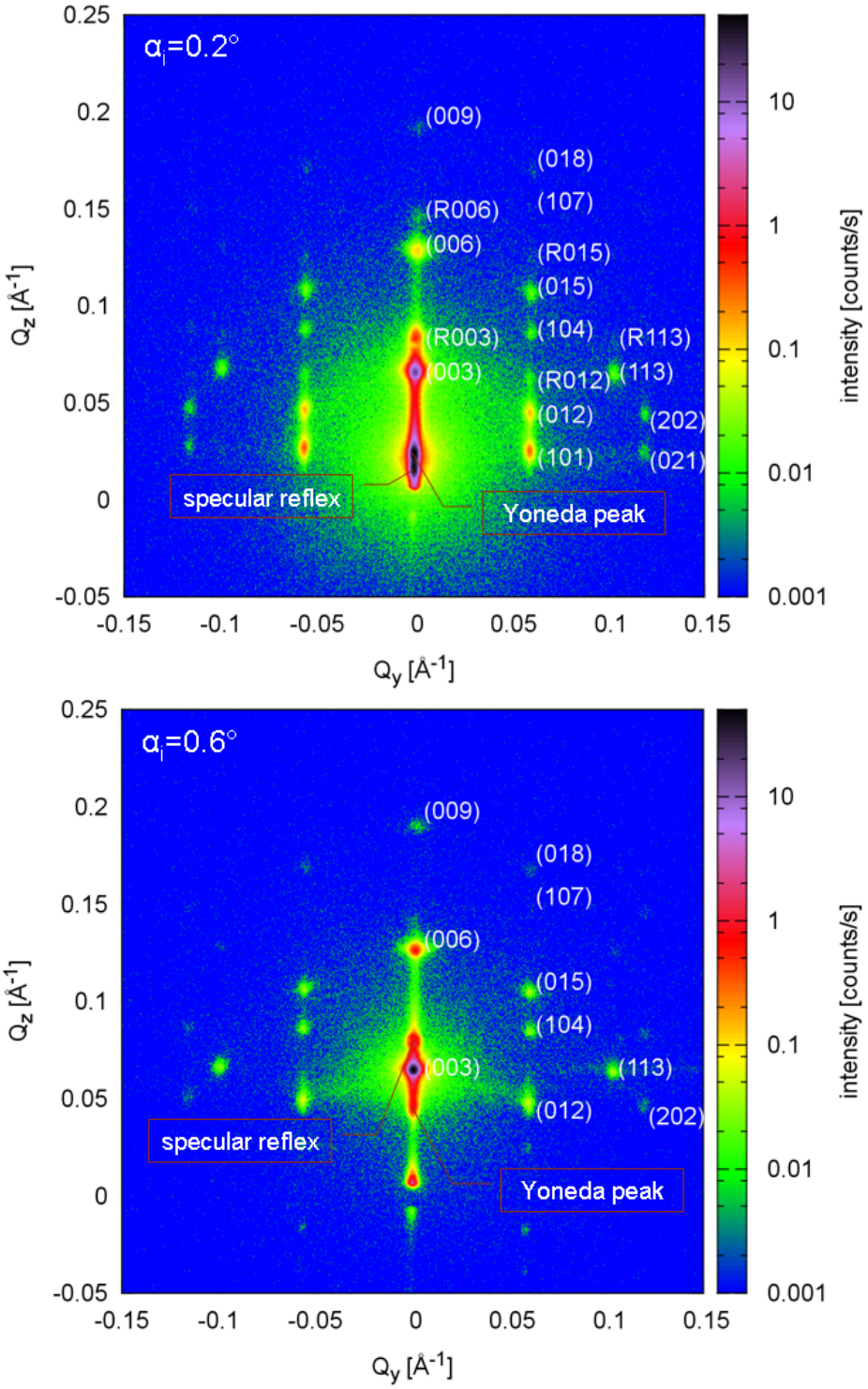

Fig. 32: *GISAXS scattering from the array of nanoparticle supercrystals at two different angles of incidence: 0.2° (top) slightly below the total reflection angle* θ_c *and 0.6° (bottom) well above* θ_c*. The diffraction spots are indexed, the peaks with index R come from diffraction of the reflected beam.*

Fig. 31 shows a cut perpendicular to the specular direction at $\alpha_i + \alpha_f = 1.9°$. In the centre, the specular reflectivity clearly dominates the curve. At the critical angles $\alpha_i = \theta_c$ and $\alpha_f = \theta_c$ the offspecular scattering is increased due to the Yoneda effect. In the range between, one can nicely fit the offspecular scattering with a Gaussian curve. The width of the Gaussian here gives the average periodicity of the lateral fluctuations, in this case the distance between the centres of the supercrystals. In this case, it turns out to be an average periodicity of 13.6 µm. When comparing to Fig. 27, one has to take into account that the coherence area is long in x-direction but narrow in y-direction, so that this periodicity only resembles the correlations along the x-direction. Neighbours that may be closer in y-direction are "invisible".

Fig. 32 shows the GISAXS pattern at two different angles of incidence. One can see a lot of diffraction peaks arising from the order of the nanoparticles inside the supercrystals. As there are thousands of supercrystals on the wafer, all in-plane orientations are present, so that the diffraction pattern observed is an average of a 2-dimensional powder-like arrangement. Only in the direction perpendicular to the surface, the supercrystals are aligned to each other. Due to this fact, e.g. the reflections (104) and (015) can be observed simultaneously, although they need a different orientation of the supercrystal in the x-ray beam. Indexing the diffraction spots yields the trigonal crystal structure $R\bar{3}$ with a lattice parameter again close to the nanoparticles' diameter.

Together with the diffraction spots one can observe the specular reflection and the Yoneda peak, both at $Q_y = 0$. At the Yoneda angle $\alpha_f = \theta_c$ there is as well increased scattering from periodicities parallel to the surface due to the enhanced wavefield, as it is observed in off-specular scattering. Especially in the bottom graph in Fig. 32 one can see the line of enhanced scattering horizontally through the Yoneda peak.

If the angle of incidence is sufficiently small, so that the reflectivity is close to 1, the diffraction from the reflected beam is comparably strong as the diffraction from the incoming beam. In this case, additional diffraction spots are visible which move with changing α_i, while those arising from the incoming beam don't move. In the top graph in Fig. 32 these peaks are indexed with "R".

It is obvious, that here we observe the inner structure of the supercrystals in the range of 10 nm with GISAXS in the y-direction perpendicular to the scattering plane, while before we looked at the arrangement of the supercrystals in the range of 10 µm with off-specular scattering in the x-direction in the scattering plane. According to eq. (1) these different ranges of lateral periodicities are accessible due to the anisotropy of the arrangement between sample surface and beam direction.

References

[1] P. Grünberg, J. Phys. Cond. Matter **13**, 7691 (2001)
[2] Physik Journal **5**, Nr. 11, p. 17 (Nov. 2006)
[3] U. Nowak, K.D. Usadel, J. Keller, P. Miltényi, B. Beschoten, G. Güntherodt, Phys. Rev. B **66**, 014430 (2002)
[4] H. Oldag, A. Scholl, F. Nolting, E. Arenholz, S. Maat, A.T. Young, M. Carey, J. Stohr, Phys. Rev. Lett. **91**, 017203 (2003)
[5] I.V. Roschin, O. Petracic, R. Morales, Z.-P. Li, X. Battle, I.K. Schuller, Europhys. Lett. **71**, 297 (2005)
[6] H. Frielinghaus, Lecture D1 of this book
[7] S. Blügel, Lecture A2 of this book
[8] J.K. Rice, "The reaction of telechelic polymers at multicomponent interfaces: A molecular loop study", Dissertation, University of Tennessee, Knoxville, USA, Dec. 2006
[9] M. Feygenson, E. Kentzinger, N. Ziegenhagen, U. Rücker, G. Goerigk, Y.G. Wang and Th. Brückel, J. Appl. Cryst. **40**, 532 (2007)
[10] D.T. Cromer, D. Liberman, J. Chem. Phys. **53**, 1891 (1970).
[11] E. Kentzinger, U. Rücker, B. Toperverg, Physica B **335**, 82 (2003)
[12] W. Babik, U. Rücker, Experimental Report FRJ-2 2002, p. 167
[13] U. Rücker, E. Kentzinger, B. Toperverg, F. Ott, T. Brückel, Appl. Phys. A **74**, S607
[14] E. Kentzinger, U. Rücker, B. Toperverg, F. Ott, Th. Brückel, F. Ott, Phys. Rev. B **77**, 104435 (2008)
[15] P. Böni, D. Clemens, M. Senthil Kumar, C. Pappas, Physica B **267**, 320 (1999)
[16] U. Rücker, E. Kentzinger, chapter D4 in IFF Spring School "Probing the Nanoworld", FZ Jülich, series "Matter and Materials", Vol 34 (2007)
[17] S.K. Sinha, E.B. Sirota, S. Garoff, H.B. Stanley, Phys. Rev. B **38**, 2297 (1988)
[18] V. Holý, J. Kubena, I. Ohlídal, K. Lischka, W. Plotz, Phys. Rev. B **47**, 15896 (1993)
[19] V. Holý, T. Baumbach, Phys. Rev. B **49**, 10668 (1994)
[20] J. Stettner, Dissertation, Christian-Albrechts-Universität zu Kiel (1995)
[21] D.R. Lee, S.K. Sinha, D. Haskel, Y. Choi, J.C. Lang, S.A. Stepanov, G. Strajer, Phys. Rev. B **68** 224409 (2003)
[22] D.R. Lee, S.K. Sinha, C.S. Nelson, J.C. Lang, C.T. Venkataraman, G. Strajer, R.M. Osgood III, Phys. Rev. B **68** 224409 (2003)
[23] S. Disch, E. Wetterskog, R.P. Hermann, G. Salazar-Alvarez, P. Busch, Th. Brückel, L. Bergström, S. Kamali, Nano Lett. 11, 1651 (2011)
[24] E. Josten, E. Wetterskog, J.W. Andreasen, E. Brauweiler-Reuters et. al., to be published